Die approbierte Originalversion dieser Diplom-/Masterarbeit ist in der Hauptbibliothek der Technischen Universität Wien aufgestellt und zugänglich.
http://www.ub.tuwien.ac.at

The approved original version of this diploma or master thesis is available at the main library of the Vienna University of Technology.
http://www.ub.tuwien.ac.at/eng

TECHNISCHE UNIVERSITÄT WIEN

JOANNEUM RESEARCH

Neuron biochip surface modification by chemical and topographical means for high througput production using Roll-2-Roll nanoimprint lithography

Master's Thesis submitted

to

Ao.Univ.Prof. Dipl.-Ing. Dr.techn. Franz Keplinger

Technical University of Vienna

Biomedical Engineering

Institut für Sensor- und Aktuatorsysteme

by

Minja Čelikić

(0948950)

in partial fulfillment of the requirements

for the degree of

Master of Science

Vienna, 3rd of March, 2017

Acknowledgement

I wish to thank to Dr. Stefan Köstler for sharing his limitless knowledge, his time, his devotion and for giving me the opportunity to work on such an interesting topic. Further I express my gratitude to Dr^{in}. Anja Haase and Dr. Martin Smolka for all constructive suggestions and support that I have got during my work at Joanneum Research. I would like thank to kind Christine Auer and Christine Prietl for introducing the techniques used within this work. My gratitude goes to all collegues, administrative and technical stuff of Joanneum Research.

I express my gratitude to my Professor Franz Keplinger for his willing acceptance to supervise my work, as well as for his constructive suggestions.

I am thankful unconditional support of my brother Nikola. When it comes to my parents, Jasmina and Mirko, I will never be able to put the gratitude I feel into words.

Abstract

This thesis describes approaches utilized for manufacture and fictionalization of a neuron biochip that is part of the project Roll-2-Roll Biofluidics. It focuses on establishing techniques needed to obtain structured surface that should promote adhesion and growth of single neural cells as a monolayer. Aiming for low cost, high throughput imprinting that is provided by Roll-2-Roll nanoimprint lithography. Prior to it, fast prototyping is needed. To that respect, high resolution high aspect ratio patterns are obtained by means of UV photolithography. Here, most of attention was given to obtain the network-like pattern of rectangular channels which is denoted under *generation 2*. The lowest feature size of 5.85 µm and aspect ratio of 3.8 was obtained for single well master. High aspect ratio serves better sensing in future use, here, it was exploited for selective coating of channels by means of spontaneous capillary flow. Due to its simplicity *generation 1* was used to compare the capillary flow within different materials.

Additionally, this work comprises measurements such as resin's autofluorescence, contact angle and wettability. Most of considered resins did fulfil the requirements of low autofluorescence, however their surface energy varies.

Contents

List of Abbreviations **v**

List of Variables **vi**

List of Figures **viii**

List of Tables **xii**

1 Introduction and Motivation **1**

2 Theoretical Background **5**

2.1 Lab-on-a-Chip System 5

2.1.1 Neuron Cell on Chip 7

2.1.2 Neuron Chip - R2R Biofluidics 8

2.1.3 Microfluidics 10

2.1.4 Wetting Transitions 12

2.1.5 Capillary Force 14

2.2 Microsystem Technology 19

2.2.1 Photolithography 19

2.2.2 Greyscale Lithography 21

2.2.3 Nanoimprint Lithography 22

2.2.3.1 Step-and-Repeat Nanoimprint Lithography 26

2.2.3.2 Roll-to-Roll nanoimprint Lithography 27

3 Materials and Methods **29**

3.1 Mastering 29

3.2 Softlithography and Imprinting 29

3.3 Autofluorescence Measurement 32

4 Results and Discussion **34**

4.1 Contact Angle of Water-Resin Interface 34

4.2 Autofluorescence of Resins 35

4.3 Generation 1 38
4.3.1 Capillary Flow within V-Groove Channels 38
4.4 Generation 2 43
4.4.1 Volume of the patterned Surface 46
4.4.2 Wetting Transitions 46
4.4.3 Roll-2-Roll Imprinting 47
4.4.4 Observed Capillary Flow Rectangular Channels 48
4.4.5 Generation 2.1 51
4.4.5.1 Capillary flow of V-shaped channels 52

5 Conclusions **54**

References **56**

List of Abbreviations

AR	aspect ratio
CE	capillary electrophoresis
DCF	dichlorfluorescine
EB-PVD	electron beam physical vapor deposition
LOC	lab on a chip
µTAS	micro total analysis system
ME	microelectronics
NIL	nanoimprint technology
PDMS	polydimethylsiloxane
PET	polyethilene terephalate
PLL	poly-l-lysine
PS	polysterene
PUA	polyurethane acrylate
R2R	roll-to-roll
RIE	reactive ion etching
SCF	spontaneous capillary force
SEM	scanning electron microscope
SR	step-and-repeat
UV	ultraviolet

List of Variables

A	area of the interface
β	apex angle of the V-cross-section channel
ΔE	energy barrier
$E_{\mathrm{C-B}}$	energy of the Cassie-Baxter state
E_f	free energy
E_y	energy of the transition state
E_{W}	energy of the Wenzel state
e	energy
$\overrightarrow{f}$	external forces
γ_{LV}	surface tension at the liquid-vapor interface
γ_{SL}	surface tension at the solid-liquid interface
γ_{SV}	surface tension at the solid-vapour interface
h	channel height
L_0	typical linear dimension
λ	typical length
$\lambda_{\mathrm{r,c}}$	typical length of rectangular confined channel
m	fluid mass
μ	dynamic viscosity
P	pressure
Pe	Peclet number
p_f	free perimeter
p_w	wetted perimeter
q	heat flux
Re	Reynolds number
t	time
$\overrightarrow{v}$	fluid velocity
$v_{\mathrm{r,c}}$	fluid velocity within confined rectangular channel
$v_{\mathrm{r,o}}$	fluid velocity within open rectangular channel

$v_{\mathrm{v,o}}$	fluid velocity within open V-shaped channel
V	fluid volume
w	channel width
z	travelled length
$z_{\mathrm{r,c}}$	travelled length within confined rectangular channel
$z_{\mathrm{r,o}}$	travelled length within open rectangular channel
$z_{\mathrm{v,o}}$	travelled length within open V-shaped channel

List of Figures

1 Preliminary design of the neouron biochip within microtitter plate . . . 3

2 Four generations of the neuron biochip planned in R2R Biofluidics project. 4

3 Four patterns of Generation 1. 9

4 Layout of the Generation 2. 10

5 Droplet within a channel of sections with different surface energies moves towards hydrophilic site. Adapted from Squieres et al. [49]. 12

6 Different wetting states on a structured surface. 15

7 Different channel cross sections. **A** Confined rectangular channel, **B** open rectangular channel and **C** open V-shaped channel. 18

8 Photolithography: **1 - 2** deposition of the resist on to wafer, **3** spinning, **4** solvent evaporation on hotplate, **5** alignment, **6** exposure, **7** developement and **8** finished master - end product of photolithography 20

9 Light intensity in the resist by a pattern of equal lines and gaps. Dashed line represents the ideal transfer, whereby the full line depicts the actual light intensity. 21

10 Subsequent steps of NIL mold fabrication. 23

11 Structural formulas: **1 Acrylate** - Trimethylolpropan $(EO)_{15}$ triacrylat , **2 Acrylate** - Bisphenol A $(EO)_{10}$ diacrylate, **3 Photoinitiator** - Esacure KL 200 (2-Hydroxy-2-methyl-1-phenyl-1-propanone), **4 Thiol** - Trimethylolpropane Tri(3-mercaptopropionate), **5 Retarder** - Benzene-1, 2, 3-Thiol [3] 25

12 Simplified working setup of Step-and-Repeat NIL. **1** UV lamp, **2** dispensing system, **3** semi-transparent mirror, **4** transparent mold, **5** substrate, **6** camera and alignment system, **7** control unit. 26

13 **1a** Resist layer rises at the border of the embossed mold, **1b** Cured resist of varying height sabotages plan-parallel position of the mold for the next imprint, **1c** increasing distance between two subsequent imprints allows parallel alignment of mold. **2a** Resist disposal just before imprinting, **2b** disposed resist - feature volume match, **2c** subsequent imprint with no restrictions 27
14 Simplified Roll-2-Roll setup. 28
15 Softlithography 30
16 Template preparation for manufacturing of metallic shim for R2R . . . 32
17 Measured contact angles of considered resins. 34
18 Fluorescence intensity vs. wavelength. 35
19 Fluorescence intensity vs. wavelength. 36
20 Bar chart of resins autofluorescence resins 36
21 Bar chart of resins autofluorescence resins. 37
22 Autofluorescence of resins. Values normalized to background. 37
23 Generation 1 master obtained by maskless lithography. 38
24 **a)** Microtomy cross section within channels of generation 1 **b)** profilometer scan. 39
25 Modelled capillary flow within V-shaped channel. Note that for 100SF-XP type G, theoretically no flow can occur for the measured angle of 81° 40
26 Capillary flow within V-shaped channel in different imprint resins. **a** JR-R2RBio-02, **b** 100SF-XP type G and **c** JR-R2RBio-02_1/23 40
27 Fluorescence microscope image: Generation 1 (from left to right: structure 1, structure 2, structure 3 and structure 4) imprints coated with Cy3 labelled protein. 41
28 Simulation of the fluid flow of structure 3 (distance between the channels 38 µm) and structure 4 (distance between the channels 17 µm) 42

29 Generation 2. **1** Darkfield and brightfield photomasks, **2** obtained Masters, M96 - hard contact exposure - smallest feature ∼8.77 µm, M109 - flood exposure - smallest feature ∼11.65 µm and M122 - hard contact exposure - with channel width of ∼5.65 µm. **3** Light microscope images with 100 times magnification of each master, respectively. 43
30 Profile of the master M96. **a)** Profilometer mesurement within pattern, **b)** microtome cross section of the imprint with BPA$(EO)_{10}$DA resin on PS substrate. 45
31 Improvement of imprinting quality by changing parameters of R2R speed v given in min/m , and pressure p against the imprinting roll in bar. **1)** Structure 1 -smallest features, **2)** Structure 2 - middle feature size, **3)** Structure, 3 largest features. 48
32 Condition for spontaneous capillary flow within open rectangular channel as a function of aspect ratio. 49
33 Capillary flow observed within confined rectangular channels. Channels confined by microscope cover glass. Note that the container diameter measures 1 mm. 49
34 Capillary flow within open rectangular channels of imprint obtained by R2R NIL (Structure 3). Note that container diameter measures 1 mm. . 50
35 Capillary flow of BSA Cy3 labelled protein within open rectangular channel. 50
36 **a)** Master of generation 2.1. **b)** Pattern with six inlets, **c)** Pattern with four inlets 52
37 **a)** Profilometry scan **b)** Microtomy cross section under light microscope, **c1)** SEM image pattern six inlets, **c2)** SEM image pattern four inlets. . 53
38 1 minute after liquid deposition: filling of the generation 2.1 pattern . . 53
39 JR-R2RBio-01 resin. Autofluorescence of four different resin thicknesses coated on a PS substrate. 61
40 JR-R2RBio-02 resin. Autofluorescence of four different resin thicknesses coated on a PS substrate. 61

41 JR-R2RBio-01_SH05/30 resin. Autofluorescence of four different resin thicknesses coated on a PS substrate.. 62
42 JR-R2RBio-02_SH05/30 resin. Autofluorescence of four different resin thicknesses coated on a PS substrate. 62

List of Tables

1 Content of imprinting resins 30

2 Generation 1 measured features. **C-D**-channel depth, **C-W** channel width, **C-C Distance** distance between channels 39

3 Feature dimensions of the dark field and bright field photomask. 44

4 Highest resolution defined through channel width (**C-W**), height represented through wall height (**W-H**) and aspect ratio (AR) obtained via different mastering approaches 45

5 Volume within rectangular channels for structure height of 20 µm. . . . 46

6 Volume within trapezoidal channels (wall tilting angle 3°C) for structure height of 20 µm. 46

7 Energy transition barrier for different contact angles. JR-R2RBio-02 imprinted against different template materials. 47

8 Pattern feature size of generation 2.1. 52

1 Introduction and Motivation

It was the middle of the 20th century when chromatography had its breakthrough as a separation technique. It did not take long to notice that reducing the diameter of the open column in liquid chromatography or capillary diameter of capillary electrophoresis (CE) brought improvement to these analytical techniques. It has been made clear that the higher the surface to volume ratio is the higher electric field could be applied and therefore better separation performance of CE was achieved.[48] First steps toward miniaturization of electrical components, has begun with miniaturization of transistors in the mid 90ies within silicon-based material. Shrinking electrical components to the microscale made the products more stable and easier to control.[39] The progress in fabrication technologies for microelectronic circuits (like fabrication of microchannels and microcavities) led to innovations in the new research field of Microfluidics. Microfluidics did not only adopt manufacture techniques from ME such as photolithography, E-beam lithography, etching, microfluidics is to be seen as an analogon to microelectronics since both techniques deal with transport phenomena of carriers an miniaturised systems caused by driving forces. Electrodynamic forces in ME is replaced with capillary or pumping force in microfluidics, whereby electrons or holes as carriers in ME are represented through carrier fluid (buffer) in microfluidics. Innovative work of Manz et al. in the beginning of 90ies has given the first glimpse of potential applications of microfluidics as fully working chemical laboratory which got the name micro total analysis systems or µTAS.[48]

Advantages of microsystems are numerous. Probably the most obvious one is that microsystems require very small sample and/or reagents. Another great advantage that might be seen as phenomeneon of the micro scale is the laminar flow due to very low Reynolds number. Since they require only small space, microchips can be produced in parallel which not only speeds up the production process, but as well makes parallel analysis possible. Due to their size these chips are portable and require low power consumption. Apart from ability to control parameters such as temperature, flow, pressure etc., one is able to obtain a fully working microchip with minimal amount of material which can reduce costs.[48] Nonetheless, microchips produced on polymers are

rather cheap and therefore suitable for medical application since it requires disposable products. Finally, a futuristic approach, it makes highly complicated chemical analysis rather easy, and by that means it will be suitable for non-experts (patients) who are in need of continuous screening systems.[22] Such decentralization of chemical analysis again reduces costs, and by ever-growing population this is a matter that has to be given regard.[22] Driven by ideas adopted from ME, microfluidics is fundamental basis of lab-on-a-chip systems and it also found its purpose in fields of chemistry, biology, medical-pharmaceutical analysis as well as in engineering.

The objective of this work is establishing techniques required to manufacture of neural cell biochips whose application is meant for drug testing. Cell responce, adhesion and growth on a surface of a biochip depends on many factors, such material biocomatibility, contact angle and wetting transitions of the given surface and finally it depends on cell properties. Geometry of biochips should be designed according to whether the cells are likely to build up a 3D structure, or rather build up monolayers etc. Neural cell consists out of cell body, dendrites and axon. Neuron cell body has a diameter of about 10-50 microns and diameter of axon ranges from few up to tens of micrometers.[7] They also have a controlled growth in terms of elongated axon and rounded cell body with branching dendrites. Cells of the nervous systems are in that way unique that they build a network and transduce signals given by action potential. They are to be considered in case of patterned surface. Surface patterning can be done both by chemical and topographical means. Choosing one or the other, or a combination of both techniques depends on application of the biochip. For example, testing growth of the cell culture by means of impedance spectroscopy does not necessarily need topographical surface modification in order to improve adhesion. Surface coating by an adherent molecule will in that case suffice. However, depending on type of cells, combination of both patterning techniques is needed. Up to date neurons have been grown on non-patterned and patterned surfaces, whereby both kinds have shown specific advantages and disadvantages.[51],[38],[32] Having non-patterned surface within microtiter well plate will host growth of neurons over whole area and it will even allow overlapping of neurons. It is clear that such arrangement is not suited for drug testing analysis by fluorescence imaging, since it is not easy to correlate the signal to a single

cell. Introducing patterned surface on the one hand deals to certain degree with this problem, on the other, however, it challenges patterning by chemical means.

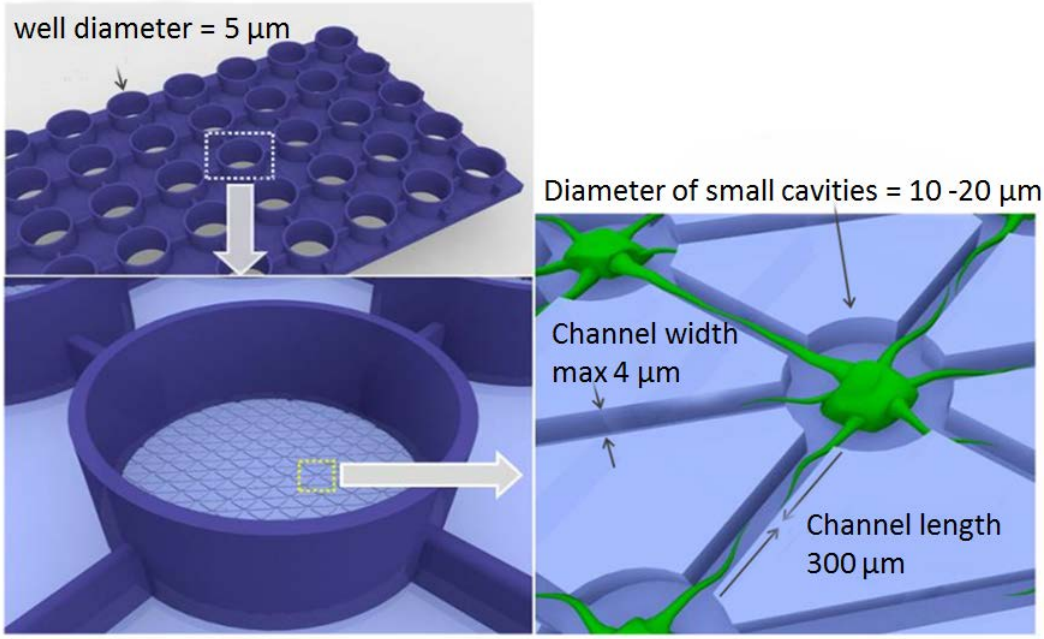

Figure 1: Preliminary design of the neouron biochip within microtitter plate

Neural cells will accommodate themselves only in certain areas where adhesion is promoted by i.e. growth molecules, certain proteins, appropriate hydrophilic behaviour etc. Chemical patterning would suffice and by that means it would be enough to deposit a layer that will promote neural growth in a certain pattern, see Figure 1. However, for better signal detection and for simplified focusing to a single cell, patterning by topographical means is required. The idea is to promote settling of neural cells within the grooves of the pattern. As the cell adhesion should only take place within the grooves and as a neural network should grow in a monolayer, upper surface of the pattern should be repellent for neurons. Patterned grooves apart from embedding neurons should allow fluid transfer. This is needed for the initial coating of the channels. Here, out of need for simplicity fluid transfer should be achieved by means of capillary flow. This simplifies the biochip in a way that there is no need for integrated component, such as a pump that controls fluid flow. Regarding cell culturing and exchange of media, the patterned structure should allow fully wettability. Development of the neuron biochip is planned to be accomplished within four stages, or four generations, see Figure 2. The first generation considers development of micro-structured surface

by means of parallel channels that are supposed to host neural cells and guide axonal growth in a predefined direction.

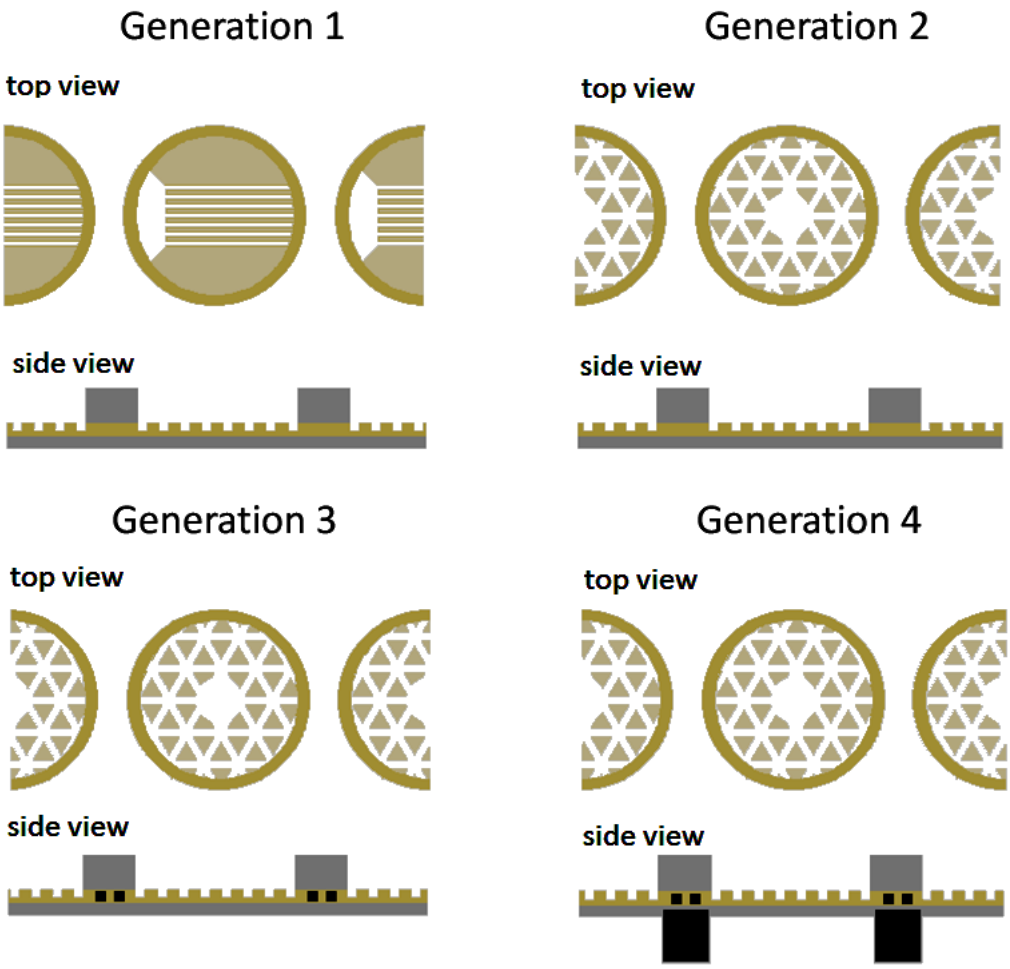

Figure 2: Four generations of the neuron biochip planned in R2R Biofluidics project.

Goal of the first generation biochip is to gain an overview how do neurons respond to a chemically and topographically patterned surface. Considering only topography, which is in this case rather simple, should give insights to cell-surface adhesion, cell-cell-connection as well as cell-cell interaction. Once such an overview is obtained, the second generation is introduced. The difference between first and second generation lies in the network-like pattern of the latter, which promotes cellular growth over the whole area of the well. In this case fluid container is placed in the very middle point of the structure allowing equal medium distribution towards the periphery. Both first and second generations are considering integration of the structured surfaces within wells of microtiter plate separately. The third generation, however, introduces a microfluidic

system that connects wells of the microtiter plate and allows perfusion of growth media, drugs and buffer. Step forward is to be done within fourth generation, where microfluidic systems inserted in third generation are equipped with an active component such as valve or pump which shall control fluid perfusion as well as sensor for monitoring of cell viability and metabolism. Such biochip enforces continuous screening and control of the cell culture within well. Producing biochips which enhance single layer neural network has great potential regarding reproducibility. Its application in drug testing is of great interest. Placing number of such biochips on a single plate enables parallel testing which is highly relevant for pharmaceutical application. Although pattern-geometry was already established there are still some challenges to overcome. One of the main concerns is how to allow neuron adhesion only within the grooves. This is, however, not an easy task on the micro-scale. The final goal is to produce these biochips on a flexible polymer foil by means of roll-to-roll (R2R) nanoimprint technique. This method has proved itself to be very precise on a large scale. High throughput is also one of the main things that are considered by this work. Ultimate goal is to establish a technique for high throughput of biochips with a rather cheap substrate such as polymer to reduce the costs. Providing low cost biochips could be considered for the developing countries.

Throughout this work in Chapter 2 the reader will acquire theoretical background about neural cell culture, basics of microfluidics and the process of producing biochips. In Chapter 3 information will be given about applied materials and methods. Results of all measurements, such as contact angle, autofluorescence, profilometry as well as theoretical calculations will be presented within Chapter 4. Finally, results will be discussed and an outlook will be given in Chapter 5.

2 Theoretical Background

2.1 Lab-on-a-Chip System

Introduced as a technique for chemical and biochemical analysis on a microscale, Lab-on-a-Chip (LOC) gains more and more importance and applications as technology evolves.[34] Merits of the miniaturised analytical systems are parallel analysis, high

throughput, controllable parameters, low sample consumption due to low volumes and low cost. LOC systems have found their application in environmental monitoring, chemical and biological analysis, DNA and protein research, point-of care diagnostics etc.[52] Exploiting the laminar flow at the microscale, microfluidics show great advantage for controlling the system and performing analytical analysis.[52] Additionally to techniques implemented from microelectronics (see chapter *Microsystem Technology* 2.2), techniques to obtain high aspect ratio were developed which is especially advantageous for sensors.[52] While for some applications LOC are equipped with sensors and pumps, needed for detection and fluid transfer, other need no additional components but only use merits of the micro-scale geometry. Such chips exploit capillary force raising from the channel dimensions.[52],[5] This not only reduces time of fabrication, but also lowers price of the final product. Applying LOC in biological analysis, or cellomics, is beneficial for various reasons. For instance, one is able to extract single living cells and monitor their growth, response to drugs or reactions to stimulus of other nature.[5] Generalizing the requirements for LOC it is expected that the device is sealed, enables working fluid transfer and is connected to sensors by i.e. microelectronical system.[52] However, real requirements of the LOC are case specific. Majority of LOC devices uses sealed microfluidic structures. This reduces the probability of contamination, fluid flow is strongly constrained by channel walls preventing fluid evaporation and ensures longer shelf-life.[52] There are several approaches how sealing can be performed.[52] These, again, are application dependent. For instance while using conformable polymers like polydimethylsiloxane (PDMS) for fast prototyping is advantageous, it is rather undesirable for large scale due to its swelling with contact to organic solvents, layering of hydrophobic molecules at the surface, instability at applied high pressures and lack of waterproof property.[52] Alternatively, sealing can be performed by nonconformal polymers such as thermoplastics, whose physical and chemical properties might be tuned in order to optimize biocompatibility as well as sensing performance.[52] One of the first approaches was to seal by glass or Si. Sealing by nonpolymer materials needs rather more complex manufacturing but has an advantage for devices that need full chemical stability and robustness.[52] Finally, some LOC do not require any sealing. Such chips rely on fluid transfer by capillary force, and are mostly used for dispos-

able detection systems - such as paper-based tests.[52] Implementing open microfluidic channels solves the issue of air bubbles trapping.[6] It is, however, of high importance that the volume of the deposited liquid does not exceed the denoted channel volume, so that performance of the open channels can be observed.[6] How the fluid connections are integrated into a chip is another important aspect. Namely, the fluidic connections serve as a link between macro and microscale.[52] These can be removable or permanently attached to the working station. Fluid connections have to fulfil requirements such as discarding cross contamination, easy to plug and detach, sustain high pressures and be chemically stable.52

Both control and sensing of the working flow, can be exhibited by use of chemical components. Again, it depends on type of sensing, kind of analyte which approach will yield optimal result. There are, however, some techniques that are often used in sensing that rely on electrical principles.[52] To name some of them, electrical impedance spectroscopy for sensing and separation techniques by means of electrokinetics, electrophoresis, chromatography etc.[52][39] Methods for selectively wetting of surface imply components integrated within LOC.[52]

The field of LOC is expanding and improving constantly. One of the aspects it covers is also decreasing of animal testing, out of ethical and economical point of view. However, culturing cell lines, and observing their reactions to certain toxins, medications yields a definite result on the cellular level, leaving the reaction of the total tissue, organs and system of organs in vivo undefined.[45]

2.1.1 Neuron Cell on Chip

While culturing neural cells on unpatterned surfaces did allow neural activation and detection, it was impossible to correlate a measured signal with single a neural cell. [51] In order to improve cell monitoring and drug screening performance, interest in culturing neural monolayers has risen over years.[51] Using patterned structures for controlling and constraining cellular growth within microchip was reported by Letourneau, back in 1975.[33] One of the first work on growing neural cells on patterned substrates was introduced by Kleinfeld et al. where they reported being able to settle cells into patterned lines of $< 10\,\mu m$ width, with improved adhesion properties provided

by protein coating.[12] These cells withstood up to 12 days on the substrate. During that time the electrical activity was observed and measured.[12] Axonal growth and compliance is adapting to the environment, with respect to chemical and topographical patterning.[38]

2.1.2 Neuron Chip - R2R Biofluidics

[1] As part of the EU project called *Roll-2-Roll Biofluidics*, biochip for investigating and drug testing on neural cells is to be developed. In scope of this work neural chip *Demonstrator 2* is to be made in few stages or generations that were already shortly introduced. Final goal of the project is to have polymer biochips on a polystyrene substrate assembled with a microtiter 96 well plate, ready for use. On the journey to the final product some issues are to be overcome. These include topographical and chemical patterning as well as choice of imprinting resin, which first of all has to be biocompatible, but also has to have low autofluorescence, adequate refractive index etc.

Ideally, topographically and chemically patterned biochip will provide monolayer forming within wanted area or channels. The top of the structures should not host any neuron cell, but this, however, can not be guaranteed since it also depends on deposition performance as well as neural cell growth/spread. Chemical coating by means of capillary force should provide optimal adherent surface for the neural cells. By that means, channel bottom and channel walls are favourable for neural adhesion/growth while the top of the pattern remains unfavourable (however still biocompatible). Adherent channels and cavities tailored to fit single axons and cell bodies respectively, give rise to single layer formation. Since drug effect on a neuron cell as well as on network of neural cells is to be monitored by fluorescent microscopy, aim of this project is to discard all "parasite" signals, which are from cells that are seeded on the top of the pattern. Avoiding unwanted signals is achieved by structures with high aspect ratio and by narrow focal plane microscopy. Two approaches have been made, one involving cell seeding onto a Matrigel (that is a 3D matrix providing network formation as

[1] Everything within this section is adapted from the project R2R Biofluidics, proposal and deliverables.

the cells were within a real tissue), and one onto protein Poly-L-Lysine (PLL) coated surface. The results have shown that for cells seeded on a Matrigel fluorescence signal was detected in 60 µm span, while by using pseudofocal mode this range decreased to 30 µm. Protein PLL coating of the surface provided 50 µm in conventional mode and 7-10 µm in pseudoconfocal mode with an estimation of 5 µm for true confocal mode. These positive results, encourage the approach to topographical patterning. Optimal patterned surfaces for neural cell adhesion are obtained within several generations. This work, however, covers fabrication of generation 1 and generation 2.

The simple geometry of generation 1 allows for comparison of different resins regarding contact angle and capillary flow within channels. The pattern consists of parallel channels with V-shaped cross-section spreading from side container that are supposed to host and guide neural cells across the biochip surface. Generation 1 comprises four different structures that differ only in distance between the V-channels and number of V-channels, see Figure 3. This allows to quantify the quality of chemical coating to exploit capillary force, depending on the distance between the channels.

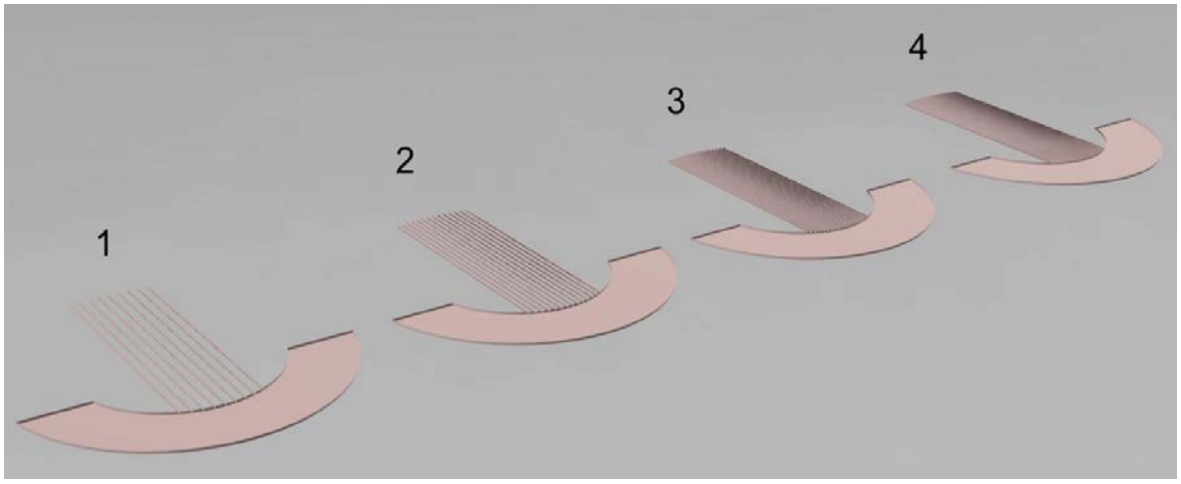

Figure 3: Four patterns of Generation 1.

Within this work most focus was given to generation 2. Its pattern comprises a network of cavities with six inlet systems that are interconnected by channels of rectangular cross-section, see Figure 4. This pattern should improve the formation if the neural monolayered network. Dimensions of cavities and channels are chosen, so that they can accommodate single neural-bodies and axons, respectively. The structures of this

generation have all the same layout, but different channel widths, namely 5 µm, 7,5 µm and 10 µm, while the total hosting area for all structures stays the same. Planned generation 2.1 was considered, where two structures were prepared, one same as generation 2 only with V-shaped channels, and the other one with cavities of four inlets, also with V-channels. For the chemical coating by means of capillary force, V-shaped channels are advantageous since they exhibit a higher capillary force.

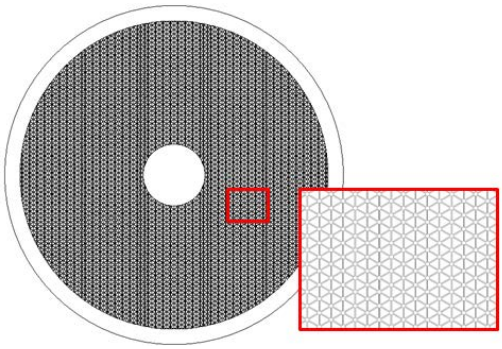

Figure 4: Layout of the Generation 2.

Pattern design was done in colaboration with biologists, however investigation of neural cell reaction designed pattern geometry has not yet been conducted. In the work of Lauer et al. it was suggested that single cells are deposited in discrete patterns with gaps of 10 µm. This improved fraction of cells that adhered properly onto patterned surface compared to the pattern of long channel line with repeatedly placed widenings (cavities) which is the case in pattern geometry of generation 2.

2.1.3 Microfluidics

Moving from macro to microscaled systems surface forces get dominant over volume forces. Consequently, inertia and gravity are suppressed by interface and capillary forces.[27] Fluid flow within micro-scaled system can be derived from continuity equation, since it can be applied to incompressible fluid, and mass conversion.[16]

$$\frac{\partial \rho}{\partial t} \frac{\partial \rho}{\partial x_i} (\rho \vec{v}_i) = 0, \tag{1}$$

where ρ is the dencity, $\vec{v}$ the velocity and t the time. In simplified case of constant density ρ and use of nabla operator $(\partial/\partial x_i)$, the continuity equation is given through:[16]

$$\nabla \cdot \vec{v} = 0 \tag{2}$$

Similarly conservation of energy yields following relation:[16]

$$\frac{\partial}{\partial t}(\rho e) + \frac{\partial}{\partial x_i}(\rho \vec{v}_i e) = P\frac{\partial \vec{v}_i}{\partial x_i} + \tau_{ji}\frac{\partial \vec{v}_i}{\partial x_j} + \frac{\partial q_i}{\partial x_i}, \tag{3}$$

where e is the energy, P the pressure, τ the total stress tensor and q the heat flux.[16]. Note that the right side of the equation (3) is given per unit of mass. For the derivation of Navier-Stokes equation 4, relation for momentum conservation is needed, and finally the equation is obtained:

$$\rho\left(\frac{\partial}{\partial t}\vec{v} + (\vec{v}\vec{\nabla})\vec{v}\right) = -\vec{\nabla}P + \mu\vec{\nabla}^2 + \vec{f}, \tag{4}$$

where $\vec{v}$ represents the fluid velocity, P on fluid exhibited pressure, μ the dynamic viscosity and $\vec{f}$ comprises all the external forces acting on fluid. Navier-Stokes equation can further be used for deriving other relations with regard to micro-scaled systems. Many of physical phenomena appearing at the microsale are represented as dimensionless numbers.[49] These are ratios of forces acting on a fluid, for example Reynolds number is relation between inertial and viscous forces, determines:[49]

$$Re = \frac{f_i}{f_\nu} = \frac{\rho v_0 L_0}{\mu}, \tag{5}$$

where ρ is the fluid density, U_0 is the fluid velocity L_0 is the typical linear dimension and μ is the fluid viscosity.[49] Since common fluid for the biochip is water based, and channel dimension are typically in the range 1-100 µm, values of Reynold number are always determined by viscous forces.[49] Roughly said, low values of Re number describe laminar flow, while the high values for Re anticipate turbulent fluid flow.[49] Other dimensionless numbers used in microfluidics are Péclet number and capillary number, describing convection over diffusion and viscous over interfacial forces, respectively.[49] Mixing of fluids on a microscale, due to laminar flow might be a challenge, letting only diffusion acting on the fluid.[49]. Péclet number is given by the ratio between convection (or movement of molecule within fluid) and diffusion:

$$Pe = \frac{U_o w}{D}, \tag{6}$$

with U_0 being the fluid velocity, w the channel width and D the diffusion. Constant movement of the fluid can be based on capillary forces arising from liquid-solid interface

forces.[49] Considering a channel of radius r with two distinct planar surfaces, one side being hydrophilic with surface tension γ_{sl}^{A}, and other being hydrophobic with surface tension γ_{sl}^{B}, a fluid droplet of length L, moves toward hydrophilic region since it is energetically favourable, see Figure 5.[49] Capillary number is then given by:

$$Ca = \frac{\mu U}{\Delta\gamma}. \tag{7}$$

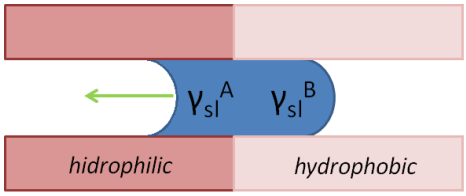

Figure 5: Droplet within a channel of sections with different surface energies moves towards hydrophilic site. Adapted from Squieres et al. [49].

Capillary forces will be discussed in more detail later on.
For Navier-Stokes equation there is no general solution, therefore, some special cases have been revised, like Couete flow, Poiseuille flow and Stockes flow.[16]

2.1.4 Wetting Transitions

Interaction between liquid drop and perfect planar surface is defined by contact angle at the interface.[43] Shape of the deposited drop results from three interface phases.[15] Namely, liquid-vapour, liquid-solid and solid vapour interface and their relation is given by Young's equation 8:[15]

$$\gamma_{\mathrm{SV}} = \gamma_{\mathrm{SL}} + \gamma_{\mathrm{LV}} \cos\theta, \tag{8}$$

where γ_{SV}, γ_{SL} and γ_{LV} are the surfaces tensions of corresponding interfaces and θ the contact angle of the liquid with the sold. However, if the surface is rough or covered with pillars, wetting transition from unwetted to wetted state can be observed. In case of an unwetted surface, or Cassie-Baxter state, air stays trapped inbetween hydrophobic pillars surface and liquid, yielding a higher contact angle than it is on a flat surface:[13]

$$\cos\,\theta_{\mathrm{C-B}} = f - 1 + \cos\,\theta, \tag{9}$$

where f is the fraction of the interface between solid and liquid and θ is the contact angle with the flat surface. On the other hand full wetting, when liquid fills the volume inbetween pillars, given under name Wenzel state, the wetted area increases and so does the wettability of the surface.[13]

$$\cos\,\theta_{\mathrm{W}} = R\,\cos\,\theta \tag{10}$$

R is here the ratio between liquid-solid interface and the total area of of the pillared surface.[13] Transition of one state to the other occurs either spontaneously - if the initial state is the state of higher energy, or induced, by changing temperature, pressure or other external forces.[13] However, the initial state of deposited droplet depends on the deposition manner, surface chemistry and topography and previous treatment of the surface.[40] In order to wet the surface, liquid has to overcome the energy barrier, the energy difference between two thermodynamically stable states, Cassie-Baxter to Wenzel state or vice versa.[13] Regarding topography, few properties have to be considered when it comes to wetting of the stripe patterned surface.[40] These are sharpness, width, height, and distance of the structured lines.[36] While for unwetted to transition state sharpness of the pattern edges does not contribute much to the wetting, effect of sharp edges has larger impact from the transition to fully wetted state. Sharp edges of the pillared structures demote wetting in comparison with smooth edges.[36] Height of the patternated structures also plays a role in surface wetting. The liquid meniscus is build between pillars but for small pillars it happens that the lowest point of the meniscus reaches the bottom of the structure. On the other hand, very high structures do not let meniscus buildup to that amount into the space between the pillars.[40] Wetting is also affected by width of the stripe, for Cassie-Baxter to transition state the wider stripe the lower contact angle is needed.[36] The larger the distance between the stripes the easier the wetting transition.[36] This is related with aspect ratio.
Due to low drop volume the influence of gravity can be ignored and free energy is given by the relation:

$$E_{\mathrm{F}} = \gamma_{\mathrm{LV}} A_{\mathrm{LV}} + \gamma_{\mathrm{LS}} A_{\mathrm{LS}} + \gamma_{\mathrm{SV}} A_{\mathrm{SV}} \tag{11}$$

A_{LS} and A_{SV} are areas of the corresponding interfaces.[36] For the pillared surface, transition per unit area, is given as the difference of Cassie-Baxter and transition state energy.[13]

$$E_{\mathrm{C-B}} = f\gamma_{\mathrm{SL}} + (1-f)\gamma_{\mathrm{LV}} + \left(1 - f + \frac{p\,h}{d}\right)\gamma_{\mathrm{SV}}, \tag{12}$$

where f is the part of surface at solid-liquid interface, h is the pillar height and p and d are pillar perimeter and density, respectively.[13] As the liquid starts penetrating into space inbetween pillars energy is modified to:[13]

$$E_y = \left(1 + \frac{p\,h}{d}\right)\gamma_{\mathrm{SL}} + (1+f)\gamma_{\mathrm{LV}} + \left(1 - f + \frac{p\,(h-y)}{d}\right)\gamma_{\mathrm{SV}}, \tag{13}$$

here y represents the depth of liquid penetration into the inter pillar space. As soon as the liquid reaches the surface bottom (y equal h) full wetted state is obtained, meaning that interface between solid and air disappears. This yields the equation for energy at the Wenzel state:[13]

$$E_W = \left(1 + \frac{p\,h}{d}\right)\gamma_{\mathrm{SL}}. \tag{14}$$

Finally, the energy barrier that needs to be overcome for a phase transition is obtained from (12) and (13):

$$\Delta E = \frac{p\,h}{d}(\gamma_{\mathrm{SL}} - \gamma_{\mathrm{SV}}) \tag{15}$$

2.1.5 Capillary Force

In Lab-on-a-Chip systems it is often advantageous to exploit capillary force rather than implementing additional components such as pumps and valves.[28] Opposite to complex systems with pumps and syringes, the flow in capillary force exploiting systems, the flow is driven by the front line of the drop in channel.[23] The derivation for the occurrence of spontaneous capillary flow (SCF) starts from the thermodynamical equation for the Gibbs free energy G:[28]

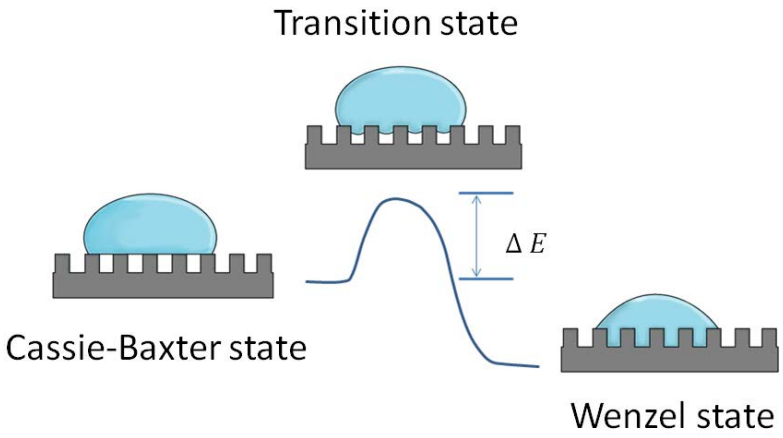

Figure 6: Different wetting states on a structured surface.

$$\mathrm{d}G = \gamma\,\mathrm{d}A - p\,\mathrm{d}V - S\,\mathrm{d}T, \tag{16}$$

where γ is the surface tension, A the interface area between liquid and solid, p the liquid pressure, V the liquid volume, S is the entropy and T the temperature of the system.[28] Assuming constant temperature and that there is no change in volume of the liquid drop, this equation reduces to:[28]

$$\mathrm{d}G = \gamma\,\mathrm{d}A \tag{17}$$

By calculating the minimum of the Gibbs free energy one obtains the equilibrium state when the A is minimal.[28] This describes the settlement state of the deposited droplet.[28] However, considering that the volume of the liquid is changing, equation for deriving the condition for SCF is obtained:[28]

$$\mathrm{d}G = \gamma\,A - p\,\mathrm{d}V < 0 \tag{18}$$

Spontaneous capillary force arises when the frontal liquid pressure is lower than the one within reservoir, or when $p \to 0$ [28]

$$\Sigma_i\,\gamma_i \frac{A_i}{dV} < 0 \tag{19}$$

i denotes all interface surfaces between liquid-solid-air, or explicit:

$$\Sigma_i \gamma_i \frac{\mathrm{d}A_i}{\mathrm{d}V} = \gamma_{\mathrm{SV}} \frac{\mathrm{d}A_{\mathrm{SV}}}{\mathrm{d}V} + \gamma_{\mathrm{SL}} \frac{\mathrm{d}A_{\mathrm{SL}}}{\mathrm{d}V} + \gamma_{\mathrm{LV}} \frac{\mathrm{d}A_{\mathrm{LV}}}{\mathrm{d}V} < 0 \tag{20}$$

Using the relation between A_{SV} and A_SL, and the Young's equation for wetting, condition for SCF is obtained:[28]

$$\frac{\mathrm{d}A_{\mathrm{LV}}}{\mathrm{d}V} < \cos\theta \frac{\mathrm{d}A_{\mathrm{SL}}}{\mathrm{d}V}, \tag{21}$$

or

$$\frac{\mathrm{d}A_{\mathrm{LV}}}{\mathrm{d}A_{\mathrm{SL}}} < \cos\theta, \tag{22}$$

where θ is the Young's contact angle. This is the general condition for SCF within homogeneous channel.[28]

Regarding dynamics, fluid flow within the channel is bound to happen, once the capillary force (23) dominates over drag force.[23]

$$F_{cap} = p_w \, \gamma \cos\, \theta - p_f \, \gamma \tag{23}$$

$$F_{drag} = \tau \, p_w \, z(t), \tag{24}$$

p_f and p_w denote wetted and free perimeter of the channel cross section and τ wall friction.[23] Further calculation of capillary flow proceeds from:

$$m \frac{\mathrm{d}V}{\mathrm{d}t} = F_{cap} - F_{drag} \tag{25}$$

where m is the fluid mass and V is the velocity of the fluid.[23] Expressing the mass through density ρ, volume through cross sectional area S_c and travelled distance z and writing the wall friction τ as a relation of viscosity μ, velocity $\mathrm{d}z/\mathrm{d}t$ and typical length λ one obtains following relation:[23]

$$\tau = \frac{\mu \, V}{\lambda} \tag{26}$$

$$\rho S_c \frac{z \, \mathrm{d}^2 z}{\mathrm{d}^2 t} + \frac{\mu}{\lambda} p_w \frac{\mathrm{d}z}{\mathrm{d}t} - \frac{p_w \, \gamma \cos\, \theta - p_f \, \gamma}{z} = 0 \tag{27}$$

Considering micro-scale, inertia can be neglected, which yields:[23]

$$\frac{z dz}{dt} = \frac{2 \, \lambda}{\mu} \sqrt{\frac{(p_w \, \gamma \, \cos\, \theta - p_f \gamma)}{p_w}} \tag{28}$$

Travelled distance within channel is obtained after integration of (28):

$$z = \sqrt{\frac{2\lambda}{\mu} \frac{t\,(p_w\,\gamma\cos\,\theta - p_f\,\gamma)}{p_w}} \tag{29}$$

Integration of obtained equation for the travelled distance (29) yields the velocity:[23]

$$v = \sqrt{\frac{\lambda}{2\mu} \frac{(p_w\,\gamma\cos\,\theta - p_f\,\gamma)}{p_w\,t}} \tag{30}$$

Obtained equation for fluid travelled distance is proportional to $\sqrt{t}$ and for fluid velocity to $\sqrt{\frac{1}{t}}$, which is coherent with the Lucas-Washburn-Rideal equation.[24] There are, however, numerous channel shapes and geometries, some of which will be discussed here. In same manner of deriving (29) and (30) equations for some specific (ideal) cases are presented. However, fabrication of sharp edges and corners is not an easy task on the micros-cale. Therefore, one deals with rounded edges within the channels. The impact of this imperfection to fluid flow raises with rising radius of curvature. General condition for capillary force reads:[29]

$$\frac{p_f}{p_w} < \cos\,\theta, \tag{31}$$

by increasing radius of curvature p_w decreases.

Confined Rectangular Channel

For computing the special case for fluid flow within a confined channel (7A), friction length λ in (29) and (30) needs to be replaced with specific parameters. Friction length can be calculated from drag force (24) and local wall friction (26), yielding:

$$\lambda_{\mathrm{r,c}} = \frac{1}{6} \frac{w+h}{\left(\frac{w}{h} + \frac{h}{w}\right)}, \tag{32}$$

which replaced in the general equation for travelled length yields:

$$z_{\mathrm{r,c}} = \sqrt{\frac{\gamma\,\cos\,\theta(w+h)\,t}{3\,\mu\,\left(\frac{w}{h} + \frac{h}{w}\right)}} \tag{33}$$

Replacing obtained λ into the velocity equation reads:

$$v_{r,c} = \sqrt{\frac{\gamma\,\cos\,\theta(w+h)}{12\,\mu\,\left(\frac{w}{h} + \frac{h}{w}\right)\,t}} \tag{34}$$

Open Rectangular Channel

Same approach is used to obtain fluid flow within open channel of rectangular cross section (7B). In this case friction length is given through:

$$\lambda_{\mathrm{r,o}} = \frac{1}{6} \frac{w + 2\,h}{\left(\frac{w}{h} + \frac{2h}{w}\right)} \tag{35}$$

Travelled distance and velocity of the fluid flow are given by:

$$z_{\mathrm{r,o}} = \sqrt{\frac{\gamma\, h\, t\, (\cos\,\theta(\frac{w}{h} + 2) - \frac{w}{h})}{3\,\mu\,\left(\frac{2\,h}{w} + \frac{w}{h}\right)}} \tag{36}$$

$$v_{\mathrm{r,o}} = \sqrt{\frac{\gamma\, h\, (\cos\,\theta(\frac{w}{h} + 2) - \frac{w}{h})}{12\,\mu\, t\,\left(\frac{2\,h}{w} + \frac{w}{h}\right)}} \tag{37}$$

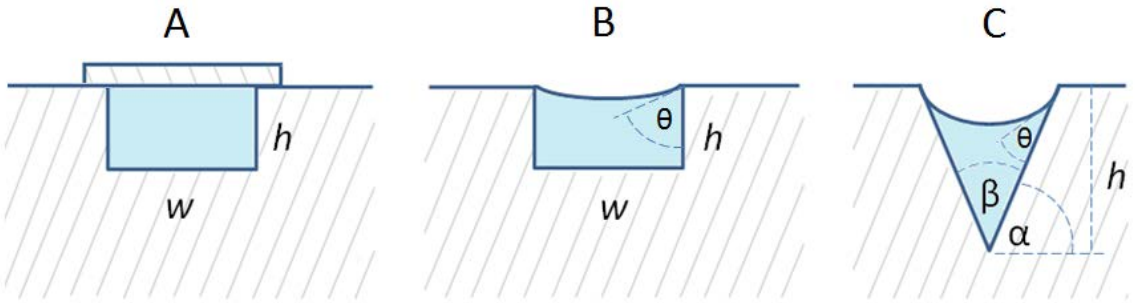

Figure 7: Different channel cross sections. **A** Confined rectangular channel, **B** open rectangular channel and **C** open V-shaped channel.

Open V-shaped Channel

For capillary force to influence liquid flow within V-shaped groove (7C) Concus-Finn condition must be fulfilled.[37],[41]

$$\theta < \frac{\pi}{2} - \frac{\beta}{2}, \tag{38}$$

where β is the apex angle of the V-groove. For the V-shaped channels, distance travelled by disposed fluid is given by:[30]

$$z_{\mathrm{v,o}} = \sqrt{\frac{(\cos\,\theta - cos\,\alpha)\gamma\, h\, t}{2\,\pi\,\mu\, sin\,\alpha}} \tag{39}$$

Velocity of the fluid within channel is calculated by integrating 39:

$$v_{\mathrm{v,o}} = \sqrt{\frac{(\cos\,\theta - cos\,\alpha)\gamma\,h}{8\,\pi\,\mu\,t\,sin\,\alpha}} \tag{40}$$

2.2 Microsystem Technology

Microelectronics, microfluidics, microoptics etc. are all comprised under term microsystem technologies. Micro- refers to a submillimeter scaled product and system refers to the fact that the system also has a function, active components that are to be carefully designed in order to have fully working product. The process of producing microchip usually starts with coating of silicon wafer by a photosensitive polymer (later referred as photoresist). This organic resin features high dimensional accuracy and sharply edge formation, which is needed for uniform layer coating of the wafer. The included photosensitive-initiator which absorbs and transfers the excitation energy to the resist molecules to trigger the polymer reaction. The viscosity of the resist is adjusted by a solvent.[31] The photoresist can be structured with different techniques. Photolithography and e-beam lithography are most common ways of producing a microchip.[31] The choice of approach depends on the desired geometry, pattern size and application of the chip. Lately, as high resolution and high throughput has been given more attention, new techniques have been developed such as nanoimprint technology.[9]

2.2.1 Photolithography

The process of projecting a pattern from a binary photomask to a photosensitive material by UV radiation, is given under the term photolithography. Suitable materials are prepolymers or polymers, in other words, negative and positive photo resist, respectively.[17] In general, photoresists are made up by resin, curing agent and solvent. While the resin type determines chemical and mechanical properties of the resist, the solvent determines the viscosity.[17] The difference between positive and negative photoresist, is that the curing agent within it, either promotes the polymerisation when it is exposed, or decomposes bonds of an already established polymer network.[17] The reaction products are soluble and can be easily removed by the developer. Negative

resist is made of a prepolymer resin, which means that it stiffens after exposure and gets insoluble for the developer.

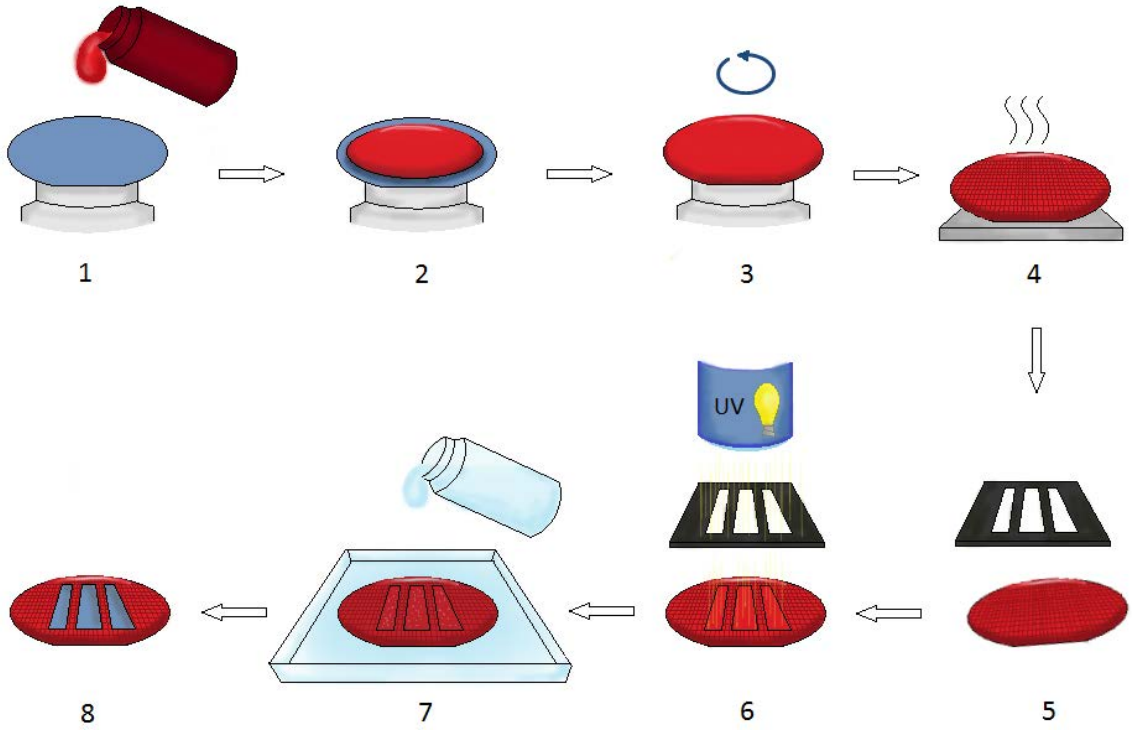

Figure 8: Photolithography: **1 - 2** deposition of the resist on to wafer, **3** spinning, **4** solvent evaporation on hotplate, **5** alignment, **6** exposure, **7** developement and **8** finished master - end product of photolithography

The depth of the features that are transferred onto resist by photolithography are determined by the resist layer thickness. While the desired thickness of solid photoresist is known, for liquid resist, thickness is given as a function of the spinning speed. As reported by Miyajima et al, smallest feature line width obtained by hard contact photolithography on a photoresisist of 23 µm thickness was 3.5 µm, which sets the obtainable aspect ratio value to somewhat 6.7.[20]

There are several techniques how photolithography may be performed, soft and hard contact lithography and step and repeat photolithography.[31] Due to diffraction effect, especially of the small structures, exposure dose is not transferred linearly to the resist, see Figure 9. This gives rise to resolution loss. The wavelength used for photo activation of the curing agent is in the range 350 - 430 nm.[31] In simplest case of having a photomask with equal width of lines and gaps, final resolution is given by:

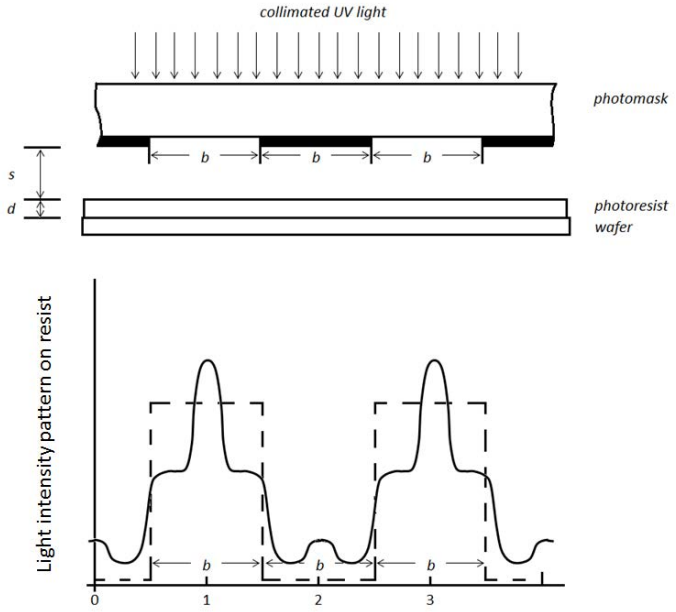

Figure 9: Light intensity in the resist by a pattern of equal lines and gaps. Dashed line represents the ideal transfer, whereby the full line depicts the actual light intensity.

$$2b_{min} = 3\sqrt{\left(\lambda\left(s + \frac{1}{2}d\right)\right)} \tag{41}$$

The achievable resolution therefore depends on the wavelength λ of the light, the gap s between mask and resist and the thickness d of the resist layer.[31] Hard contact photolithography features no gap between photomask and resist, meaning that higher resolution can be achieved. However, tight contact contributes to mask damage, since the mask gets contaminated by the resist.[31] To avoid mask damage, soft contact lithographyncan be applied that introduces defined space s between resist and mask.[31] This, of course, lowers the final resolution.

2.2.2 Greyscale Lithography

Due to binary property of a photomask, features made by photolithography are limited to two dimensions.[4] Greyscale lithography controls position by varying the exposure dose.[25],[4] By this means this technique is able to perform 2.5D patterning of photoresist. This process needs no photomask, but uses a virtual mask - which is a computer model that codes the right position and exposure dose for the laser beam.[4] There are

several techniques that can provide writing into photoresist based on software given information. These are: e-beam lithography, focused-ion beam and laser lithography.[4] Transfer from the virtual mask onto photoresist relays on optical systems needed for beam projection and focusing. Quality of relief obtained by maskless lithography are reflected in resist profile which depends on depth of focus and achievable resolution.[10] Resolution is the smallest feature - linewidth - that can be transferred as a feature in a resist is given with following relation:[10]

$$R = k\left(\frac{\lambda}{NA}\right), \tag{42}$$

where R stands for resolution or smallest printable linewidth (also called critical dimension), k is factor of proportionality, λ wavelength of incoming beam and NA numerical aperture optical system ($NA = n \cdot \sin\alpha$).[42] Depth of focus, on the other hand, is described as spread of points where focus of acceptable errors can be applied. Resist profile is determined by linewidth, tilting angle and depth of the feature within resist and these are the three parameters which are specified within computer model that one wants to transfer onto the resist.[10]

2.2.3 Nanoimprint Lithography

Technology of manufacturing features on a sub-micron scale called nanoimprint lithography (NIL) was introduced in the mid 90ties.[11] Advantage of embossing technique compared to photolithography lies in high resolution and high througput at low cost.[9] NIL technique implements manufacturing of a working stamp (mold) which is pressed against the curable resist in order to mechanically transfer features onto it.[19] Mold in the NIL technology has the same roll as photomask in photolithography that is feature transfer onto curable resist. Properties that mold should comprise are hardness and high mechanical strength.[18] However, overall flexibility and local rigidity of he mold are ideal properties since such a mold conforms very well on the large scaled flexible substrate.[18] Requirements for the resist are that it is deformable and that it can be hardened in order to maintain the imprinted features.[18] There are two approaches for manufacturing features on sub-micron scale by NIL. The first one is classified as thermal nanoimprint technology use polymers that were liquidized by increasing the temperature over its glass transition temperature so that the feature of the mold can

be embossed into it.[11] Due to high viscosity of polymer, the process of imprinting has to be done under high pressure.[18] The higher the temperature, the less viscous is the resist. This allows embossing at lower pressure, improvising the separation of mold and imprinted resist. However, high temperature also effects higher expansion difference of two materials with different thermal expansion coefficients - like mold and resist, which causes alignment problems especially on large scale.[18] After the resist has been cooled the mold gets lifted and residue of resist within structured surface can be removed by etching.[11] Resist residue arises from the fact that the mold does not get in contact with the substrate. This could damage both mold and substrate.[11] The second approach called step-and-repeat nanoimprint lithography (SR-NIL) uses UV-curable resist, and it requires a transparent mold so curing can take place. This method is classified as UV-based nanoimprint lithography (UV-NIL) and it can be performed under room temperature.

Mold Fabrication

Choice of materials used for mold fabrication depends on type of NIL technique. Namely, for the thermal NIL where high temperatures, matching thermal expansion coefficient between mold and resist are needed, to restrict damages due to stress forces during cooling process.[18] For this instance, Si mold against silica substrate is a good match.[18] Si mold is fabricated by means of lithographic techniques such as photolithography for larger features, or electron beam lithography for patterning of smaller features. Metallic, or masking layer is deposited onto patterned surface. With the lift-off process, the sacrificial layer is removed, and a layer of patterned mask is obtained on Si substrate. To fabricate relief features reactive ion etching (RIE) is utilized to remove unmasked Si, see Figure 10.

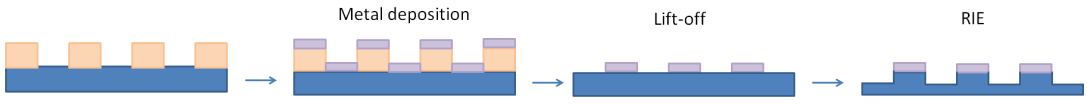

Figure 10: Subsequent steps of NIL mold fabrication.

A similar method is used for fabrication of mold for SR-NIL. Nevertheless, one of the material requirements for SR-NIL is that the mold is transparent. Therefore, quartz

or silica are commonly used.[18] Even though SR-NIL has an advantage of working under room temperature, the difficulty arises due to charging effect that is an artefact of non-conductivity dielectric material that occurs during e-beam lithography.[18] This effect of charging can alter the e-beam and reduce resolution and pattern alignment. To avoid this, several approaches have been proposed, one of which considers coating of the quartz substrate by nm-scaled layer of metal, such as chrome, prior to spin coating of the e-beam resist. Benefit of the Cr layer, is that it serves as etch mask after the lift-off process.[18] Another approach is deposition of a conductive oxide layer, which not only helps e-beam lithography process improvement, but also assures the investigation of the structures with scanning electron microscope.[18] Regarding mold-imprint interface, it is of great advantage that the surface of the mold is not adhesive, in order not to damage imprint nor mold during detaching it from the imprint. For this instance several techniques have been proposed: mixing a release agent within the SR-NIL resin, coating of low surface-energy layer onto the mold or using materials of *a priori* low surface energy for mold.[18]

NIL Resist

Requirement for an optimal NIL resist is that it deforms upon mechanical stress while embossing the mold. The Young's modulus of the resist should be lower than the one of the mold material.[18] Regarding pressure needed to emboss the pattern into the resit, it has to be greater than the resists' shear modulus.[18] Since imprinting time is an important parameter, low viscosity of the resist is favourable.[18] Assuming that the resist during relief of the mold behaves as a Newtonian fluid, one can derive the time that is needed to fill half of the pattern height by integrating (43) for pressure P obtained from the Stefan's equation for the squeezed flow between planar disks of radius R:[50]

$$P = -\frac{3\pi R^2}{4h_0^3}\frac{\mathrm{d}h}{\mathrm{d}t}\eta_0 \tag{43}$$

$\frac{\mathrm{d}h}{\mathrm{d}t}$ is the feature filling velocity and η_0 is the fluid's viscosity.

$$t_{1/2} = \frac{9\pi R^2 \eta_0}{16 F h_0^2} \tag{44}$$

The equation (44) states that the time needed to fill half of the relief hight scales quadratic with the disc radius and linearly with viscosity, showing the advantage of imprinting nanoscale compared to large scale patterns.[50],[18]

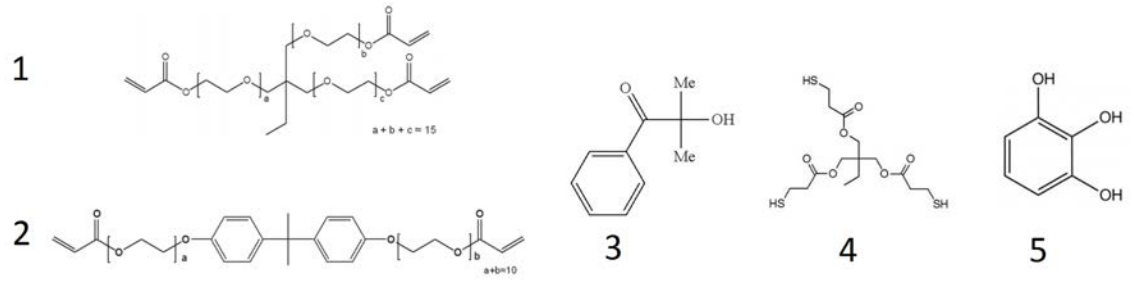

Figure 11: Structural formulas: **1 Acrylate** - Trimethylolpropan $(EO)_{15}$ triacrylat , **2 Acrylate** - Bisphenol A $(EO)_{10}$ diacrylate, **3 Photoinitiator** - Esacure KL 200 (2-Hydroxy-2-methyl-1-phenyl-1-propanone), **4 Thiol** - Trimethylolpropane Tri(3-mercaptopropionate), **5 Retarder** - Benzene-1, 2, 3-Thiol [3]

UV curable resists are made from monomeric solutions and, therefore, they fulfil the requirements of low viscosity and low elastic modulus prior. These resists are usually composed of acrylates and photoinitiators. Common components of UV-curing NIL resist are shown in Figure 11a Depending on application, shelf life time or other requirements of the resist additives can be added. Polymerisation of the resist occurs upon exposing it to UV-light. Crosslinking of monomers happens after the photoinitiator, which makes up 0.1 to 5% of the solution gets activated by UV light.[47] Radicalized photoinitiator delivers the energy needed for combining the monomers. By means of cross linking and polymerization, the resist becomes stiffer and more rigid which makes it capable of preserving the imprinted features and easier to separate the mold.[18] There are some resists that need no addition of photoinitiator, whose curing is governed by other means of polymerisation such as thiol-ene- and electron donor-acceptor-reactions.[47] Such resists show better optical clarity and better photostability once the final product is obtained. Due to added thiols, it comes to rapid polymerization as the resist get exposed to UV light, while isolated from light no spontaneous reaction will happen.

2.2.3.1 Step-and-Repeat Nanoimprint Lithography

Method of patterning large areas by sequential imprinting of resist can be performed by means of step and repeat UV lithography. There are two different approaches how the resist can be deposited, one uses pre-spin-coated wafers while the other has uses special dispensing system prior to every printing event.[53] Essential components of these methods are template mold, alignment and UV-exposure system.[53] While merits of this technology are high throughput, as well as simplified deposition of polymer onto a substrate, it raises the requirements of NIL resist stability.[35] The working principle of the step-and-repeat machine is presented in Figure 12. The mold is held by a movable stage which is coupled with the camera and laser equipped alignment system.

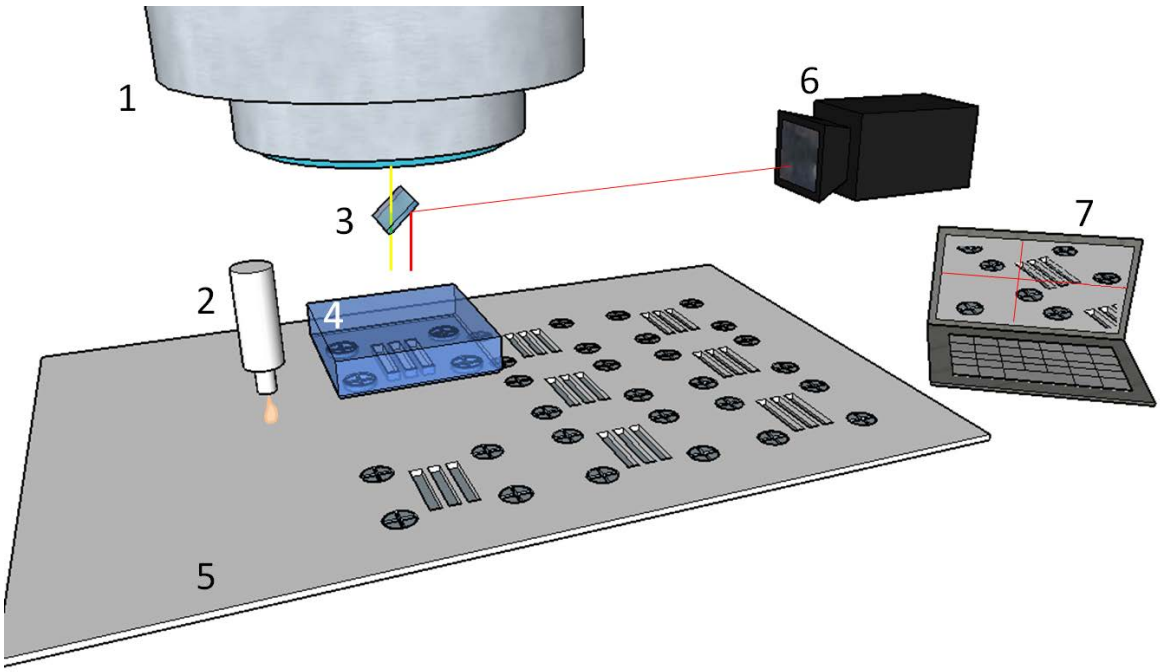

Figure 12: Simplified working setup of Step-and-Repeat NIL. **1** UV lamp, **2** dispensing system, **3** semi-transparent mirror, **4** transparent mold, **5** substrate, **6** camera and alignment system, **7** control unit.

Using a mold-template for multiple imprinting on a large wafer faces two difficulties. First sticking at the mold imprint interface during detaching and second, differences in resist layer thickness at the edge of the imprinted feature, Fig. 13.[35] Solutions for the first issue are already mentioned above (see *Mold Fabrication*).

For SR-NIL the density of transferable patterns on large wafers depends on resist

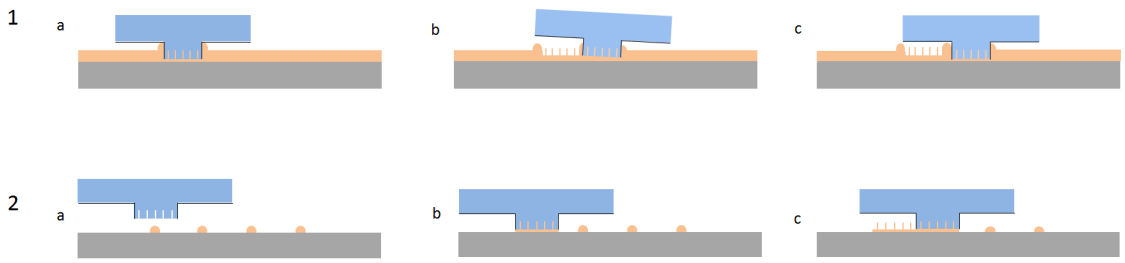

Figure 13: **1a** Resist layer rises at the border of the embossed mold, **1b** Cured resist of varying height sabotages plan-parallel position of the mold for the next imprint, **1c** increasing distance between two subsequent imprints allows parallel alignment of mold. **2a** Resist disposal just before imprinting, **2b** disposed resist - feature volume match, **2c** subsequent imprint with no restrictions

accumulation residue.[9] Method key is dispensing just the right volume needed to imprint the features from he working stamp.[9] As reported by Otto et al. SR-NIL is a technique capable of producing over thousand imprints without cleaning the template mold.[35] Since SR-NIL uses precoated wafers, in comparison to subsequent resist dispensing, it reduces the total time needed, especially it advantageous as high throughput technique.[35]

2.2.3.2 Roll-to-Roll nanoimprint Lithography

The need for continuous high throughput imprinting has brought another branch of UV nanoimprinting technique, roll-to-roll nanoimprint lithography (R2R NIL).[46],[26] R2R technique successfully provides resolution achievable with standard NIL techniques and moreover is able to perform imprinting of large areas in a continuous manner, which is a huge merit for high volume production.[26] Another advantage of R2R compared to other nanoimprinting techniques, is the manner of pealing off, rather than pulling off, the mold from the imprinted structure which lowers the chance of damaging the imprint or mold.[26] There is, however, a limitation of the aspect ratio that can be achieved by Roll-2-Roll imprinting. As reported by Yoshikawa et al, the highest aspect ratio achieved so far is 5.[21]

A mold used in R2R may contain different patterns (of similar pattern depth), so different structures can be manufactured simultaneously. Preferred positioning of pattern

along the molding roll often depends on the pattern geometry. Final resolution and pattern fidelity of the imprinted structures depend on quality of the mold, which is placed on a rolling cylinder in R2R setup.[26] Materials that can be utilized as mold spreads from polymeric materials to metallic shims such as nickel or aluminium.[26] Choice of mold material depends on resolution and durability requirements for each process.[26] Nevertheless, the choice of the resist material strongly depends on the desired future application of imprinted structures.[26] Most important parts of the R2R setup are coating station, working-stamp-cylinder (mold), UV light source. The setup is further equipped with a number of additional Roll-2-Roll systems that assure continuous movement of substrate toward and from the UV-exposing station, Fig. 14.

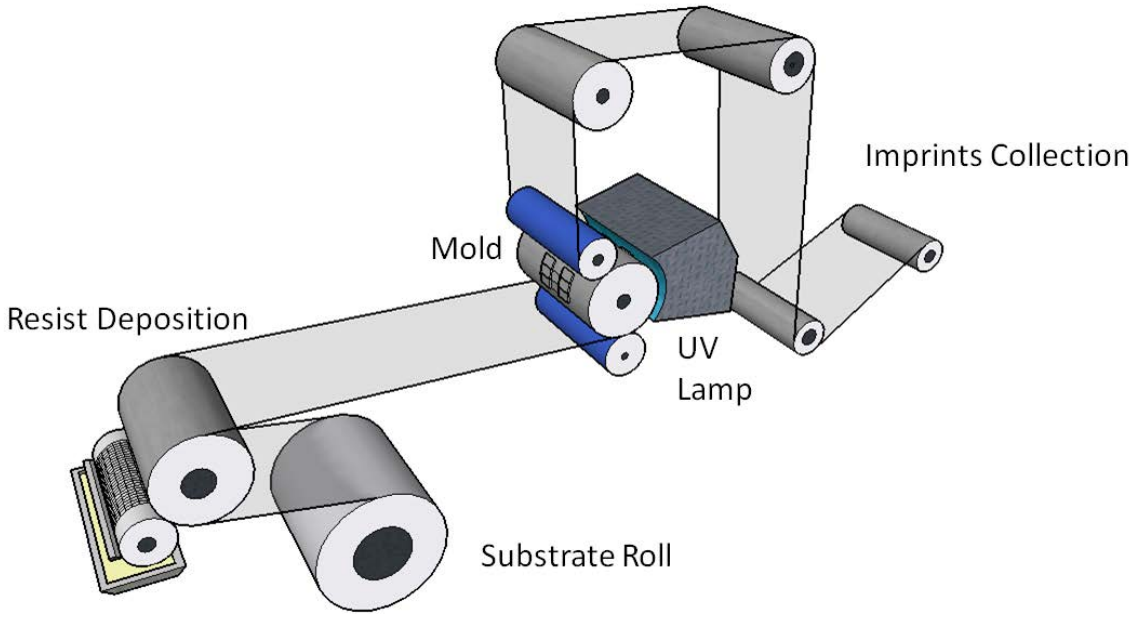

Figure 14: Simplified Roll-2-Roll setup.

The process of imprinting starts with resin deposition. There are several methods how resins can deposited. To mention some, slot-die coating, knife coating, gravure printing.[44] Goal of coating is to continuously and uniformly deposit a layer of resist onto a flexible substrate. The exposure happens simultaneously with engraving the pattern from te mold to the resist on substrate. Varying time of exposure is done by varying the speed of R2R process. As it has been reported, speed for successful imprinting can be adjusted to 1 to 20 m/min.[44]

3 Materials and Methods

3.1 Mastering

Prior to photolithography cleaning of the wafer was performed by O_2 plasma treatment. Plasma pretreatment also improves the resist to wafer adhesion. Coating of the negative resist Ordyl SY320 (ElgaEurope) was performed by hot lamination by Photopro Laminator at 100°C whereby deposition of resist AZ 9260 (MicroChemicals) positive resist was done by spin coating. In order to reduce the formation of air bubbles, the resist was deposited directly from the original container.[31] Spin parameters for the desired layer of $\sim 20 \mu$m thickness were set to 500 rpm for 30 s, acceleration was set to 100 rpm/s. Subsequently, the wafer was put on hotplate at 95°C for 3 min in case of Ordyl SY320 and 95°C for 15 minutes in case of AZ 9260 in order to evaporate the solvent of the resist. Exposure to the UV-light was done by an EVG620 aligner equipped with mercury arc lamp with band from 350 to 450 nm. The exposure dose varied from 400 mJ/cm^2 to 7000 mJ/cm^2 depending on type of resist and desired resist layer thickness. For the removal of depolymerized resist, MIF 826 developer was used for AZ 9260 positive the resist and PGMEA developer for Ordyl SY320 negative resist. After the soluble part of resist on the wafer was totally removed, the master was taken for the profilometer measurement to check, uniformity and obtained resist layer thickness. This was done via Dektak 150 (Veeco) contact profilometer. Stylus of radius 2.5 µm with force of 3 mg was used for the measurement within 65 µm vertical range.

3.2 Softlithography and Imprinting

After the master width the desired profile has been obtained, a polydimethylsiloxane (PDMS) mold was made. PDMS (liquid) was mixed with a hardening agent in 10:1 mixture ratio. For 4″wafer $\sim$40 g of PDMS and $\sim$4 g of hardening agent was needed. After mixing, the solution was left in a low vacuum chamber to eliminate air bubbles. After approximately 2 h, the uniform solution of PDMS and hardening agent was

poured over the master within a petry dish, and was hardened at 45°C over night, (Figure 15).

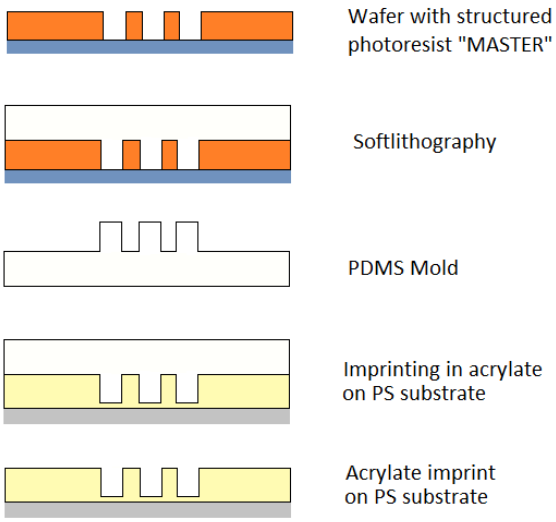

Figure 15: Softlithography

Solidified PDMS mold, which has the exact opposite structure than the master, was deattached from the master and further used as a stamp for making imprints. Imprinting resin that contains photo initiator which causes polymerisation of the material under UV light was drop deposited onto a polystyrene substrate (PS refractive index $n = 1.5916$)[2] of 190 µm thickness. A UV-lamp Waldmann (MediLux) with 315–380 nm bandwidth was used to activate the initiator. In this work, four different imprint resins were prepared, see Table 3.2.

Sample Code	**Composition**				**Refractive Index**	**UV curing**
	Acrylate	Thiol	Initiator	Retarder		
JR-R2RBio-01	$TMP(EO)_{15}TA$	-	1% KL200	-	1.471	10 min
JR-R2RBio-02	$BPA(EO)_{10}DA$	-	1% KL200	-	1.516	10 min
JR-R2RBio-01_SH05/30	$TMP(EO)_{15}TA$	30% Di-PETMP	1% KL200	0.05 % Pyrogallol	-	10 min
JR-R2RBio-02_SH05/30	$BPA(EO)_{10}DA$	30% Di-PETMP	1% KL200	0.05 % Pyrogallol	-	10 min

Table 1: Content of imprinting resins

Nickel Stamp

A metallic stamp was manufactured by e-beam physical vapour deposition process (EB PVD) was utilized. The process starts with an imprint on a glass substrate utilizing a resin with very good adhesion to it, in this case OrmoStamp (Microresist Technology). Prior to imprinting, glass substrate was cleaned in following manner: 1 h on a hotplate at 200°C followed by cleaning per hand using a tissue with acetone and isopropanol. After these preliminary cleaning methods the glass substrate was treated by oxygen plasma for 10 min. Curing of the OrmoStamp was performed under Waldmann UV lamp for 10 min with PDMS mold on it followed by 5 min without PDMS mold. The glass wafer with imprinted structure was than placed on the sample holder within the PVD-vacuum chamber. Air from the chamber was pumped out overnight to get very high vacuum (1.3 x 10^{-6} mbar) to achieve the required mean free path. To assure that the deposition of the Ni atoms over the whole substrate surface is uniform, the sample holder was set to rotation of 4 rpm. Ni deposition in the beginning was set to a low rate (0.7 Angstrom/sec), since the fine pattern structures are to be coated smoothly and uniformly. This was done with 64 mA. After a layer of approximately 20 nm was obtained, the power was raised for 2%, 85 mA, which gave a rate of 3 Angstrom/s. Deposition of Ni atoms was done until ∼200 nm was obtained. After the sample (with additional layer) was taken out of the chamber, a Galvanic cell was prepared to form a thicker and more robust Ni stamp. Substrate (anode) was placed into a tub full with filtered electrolyte against a Ni shim (cathode). The voltage was set to 4 V and current first to 0.1 A, afterwards it was raised to 0.2 and finally 0.25 A. After about 20 h a Ni stamp of ∼400 µm thickness was obtained.

Preparation of Shim for Roll-2-Roll

Features from the PDMS are imprinted into undiluted polyuretane acrylate 8210 (PUA) with 1-2% KL200 on PET substrate (refractive index $n = 1.636$)[1], see Figure 16.
UV curing time was set to 10 minutes. Obtained imprint, was dipped in Optool for 1 minute. The imprint was then left in water vapour for 1 h. Afterwards, the imprint was dipped into perfluorehexane for 10 min. This imprint was further used as a stamp

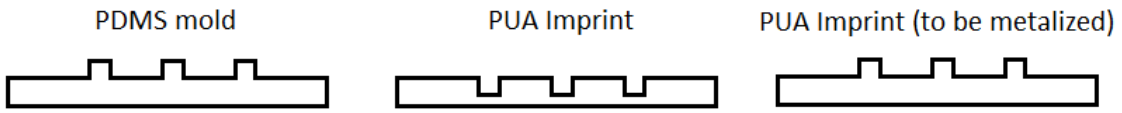

Figure 16: Template preparation for manufacturing of metallic shim for R2R

for making imprint with mixture of PUA 8210, HDDA and HFPO on a PET substrate of shim size (25 cm times 60 cm), curing time by UV light 10 minutes which was then metallized. Metalization of the PUA imprint was performed by sputtering, firstly with a 5 nm Cr layer as an adhesive layer followed by Al layer of 50 nm.

Roll-2-Roll Imprinting

Automated imprinting was done on R2R pilot mashine. Resin JR-R2RBio-02 ($BPA(EO)_{10}DA$) was deposited onto a Melinex PET 125 µm substrate by gravure printing of 60 µm and effective resin layer thickness was estimated to be around 30 µm. While the setup was running, two parameters were varied. These are the pressure against the UV-roll and the speed, from 0 to 0.1 bar and from 1 to 2 m/min, respectively. PET substrate was unwind from the roll and coated by the resin from the upper side. Tension set at this roll was set to 70 N. The UV curing takes place on the roll, where the tension was set to 100 N. The imprints on PET foil wind around the roll of 70 N tension, also from the upper side.

3.3 Autofluorescence Measurement

Measurement of the resins' autofluorescence was performed by TECAN infinite M200 PRO. Resins of ∼30 µm thickness were deposited on the PS substrate by spin coating. Samples were then attached to the Greiner black microtiter plate by double side adhesion foil. Black microtiter plate was used to exclude possible cross fluorescence between wells. Dilution series of Dichlorofluorescine (DCF) solution was prepared as tenfold series in concentration range from 10^{-7} to 10^{-12}M, in TRIS buffer of pH 8. To cover the well bottom (PS substrate) completely, 30 µl was taken. The goal was

not to have a too much height difference between the samples and DCF dilution, in order to optimize z-position of the PMT (photomultiplier tubes) detector. Apart from resin samples and DCF, measured were also empty polystyrene foil (190 µm) and TRIS buffer. The excitation wavelength was set to 480 nm, while the emission wavelength was recorded in the range from 520 to 650 nm in 3 nm steps. The gain was calculated from the well with expected lowest intensity and the one with highest and was than set to an optimal value.

Second approach of checking on autofluorescence is by means fluorescence microscopy. Each resin was deposited onto a PS substrate using film applicators of 2 and 4 mil * in combination with metallic spacers. By that means layers of thicknesses 55, 130 and 170 µm were obtained. Resins' contrast to PS substrate was observed by fluorescent microscope.

*thousandth of an inch (1 mil=25.40 µm)

4 Results and Discussion

4.1 Contact Angle of Water-Resin Interface

Intended for cell hosting, patterned NIL have to be wettable. Measured values of contact angles of various NIL resins coated on different substrates are given within bar chart in Figure 17.

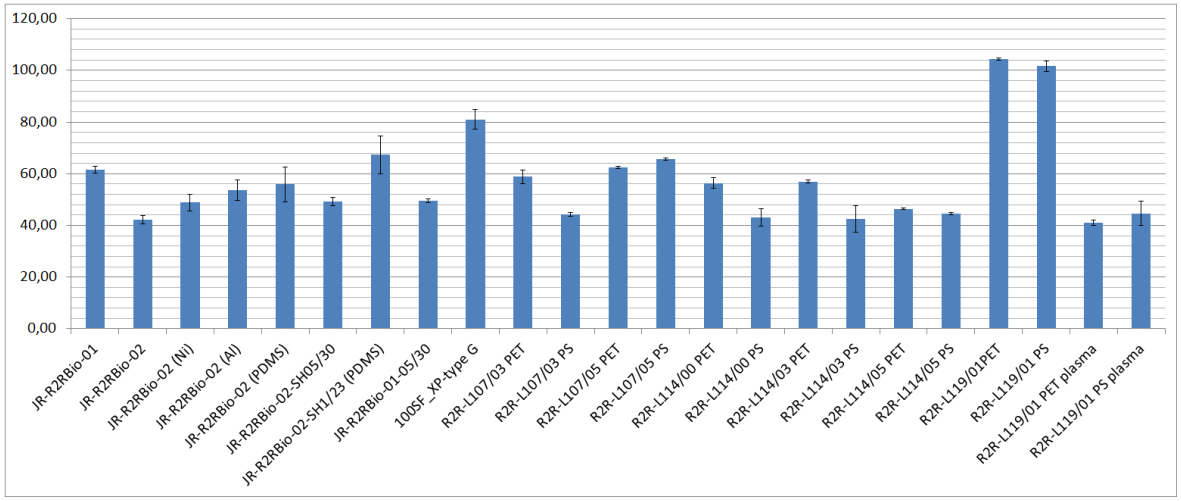

Figure 17: Measured contact angles of considered resins.

Contact angle with high value of standard deviation of resins cured against PDMS suggests, that the obtained surface is rather heterogeneous. This is caused by porosity of the PDMS, which lets air in during curing. Highly reactive oxygen within air bonds locally to free radical coming from initiator within resin. This undermines the polymerisation of the resin. Resin JR-R2RBio-01 cured under inert gas showed the value of ∼61°, while its version with addition of thiol (30%) and pyrogallol (0.05%) yielded ∼49°. JR-R2RBio-02 showed its high hydrophilic property, ∼42°, when cured under inert N_2 gas. However, curing against other materials such as nickel, aluminium or PDMS increases the contact angle to ∼48°, ∼42° and ∼56°, respectively. Modified JR-R2RBio-02 resin with addition of 30% thiol and 0.05% pyrogallol as it is the case for the resin JR-R2RBio-02_SH05/30 yields higher contact angle at the interface with water droplet ∼49°. Same resin with different percentage of contents, 23% thiol and 1% pyrogallol, cured against PDMS in air environment showed interface contact angle of ∼67°. Resin with code name 100SF-XP type G (MicroresistTechnologies) showed

contact angle ∼81° after curing against PDMS in air. All other resins (prepared by MicroresistTechnologies), cured under inert gas environment, yielded contact angle values in range between 40° and 65°, with exception of R2R-L119/01 both PET and PS substrate where the surface showed hydrophobic behaviour. Impact of plasma treatment shows high improvement in reducing contact angle (more than 60° decrease for R2R-L119/01).

The real (advancing) contact angle was rather difficult to determine, since the water drop shape had tendency to change fast after being deposited onto the surface. High measurement fluctuation is also the reason why the same resin (on different substrates) yields different contact angles. Therefore, contact angle measurement, gives a rough idea about hydrophilic properties of resins.

4.2 Autofluorescence of Resins

The results of autofluorescence measurements of resins are depicted in Figures 18 and 19. Maximum are presented as bar chart within Figures 20 and 21.

To compare samples, data was normalized to background, which was polystyrene substrate. The bar chart in Figure 22 gives an overview of autofluorescence of different

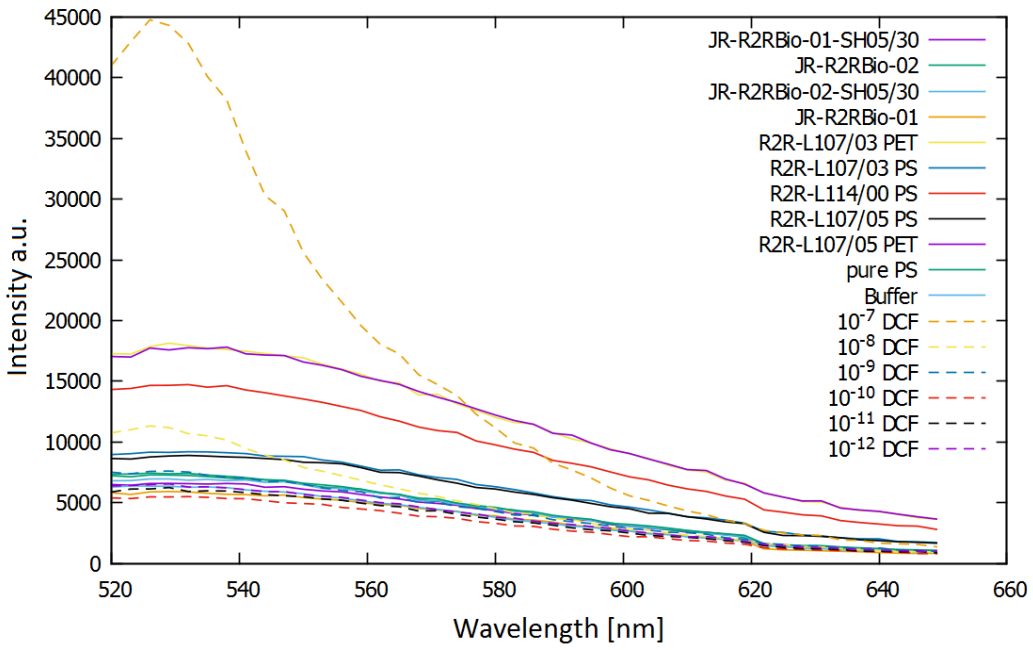

Figure 18: Fluorescence intensity vs. wavelength.

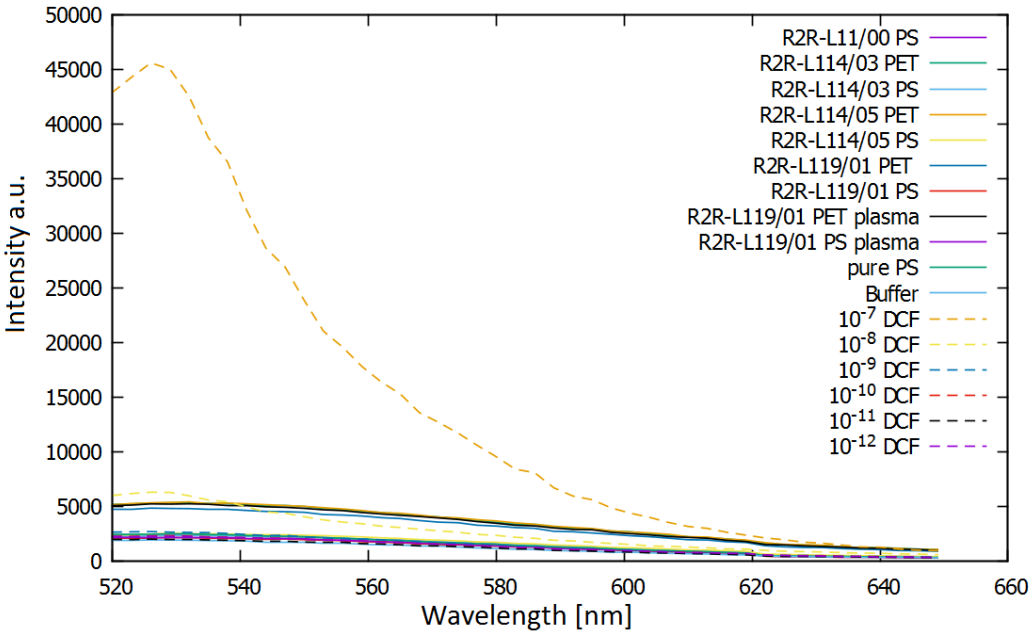

Figure 19: Fluorescence intensity vs. wavelength.

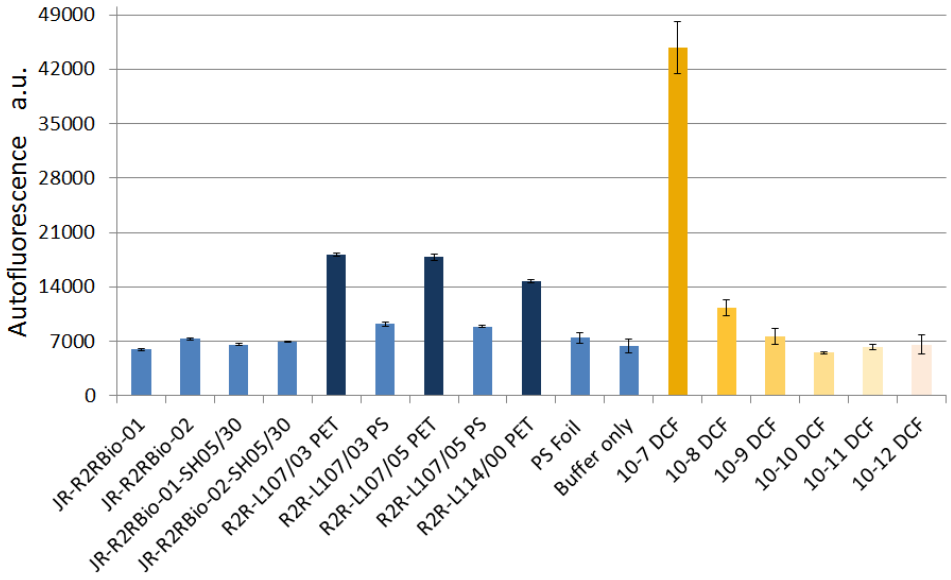

Figure 20: Bar chart of resins autofluorescence resins

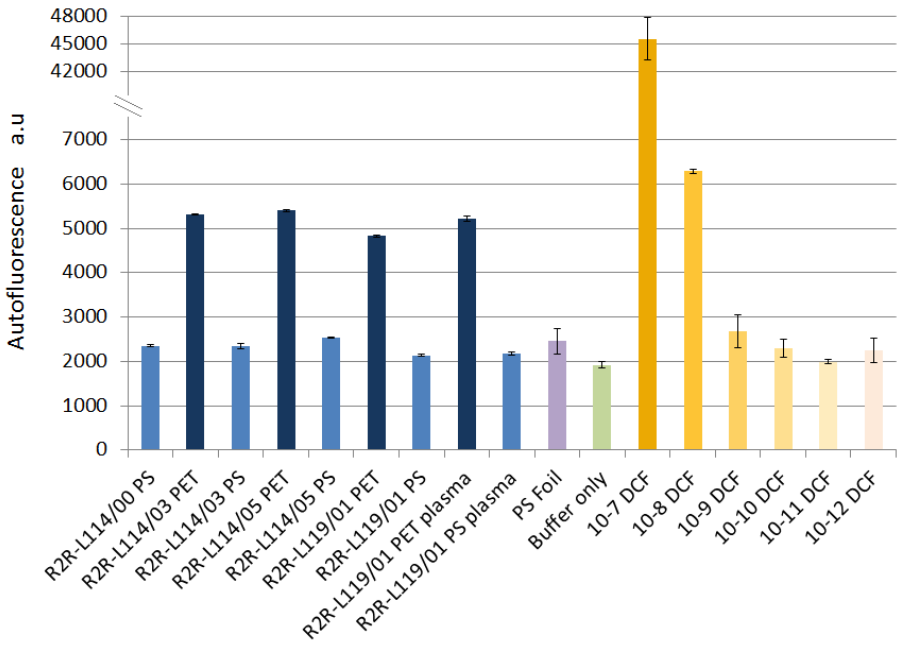

Figure 21: Bar chart of resins autofluorescence resins.

resins coated on PS or PET substrates. It is to be deducted that these resins show autofluorescence in range of the fluorescence of the PS foil, at least when the resin layer thickness is lower than 30 µm.

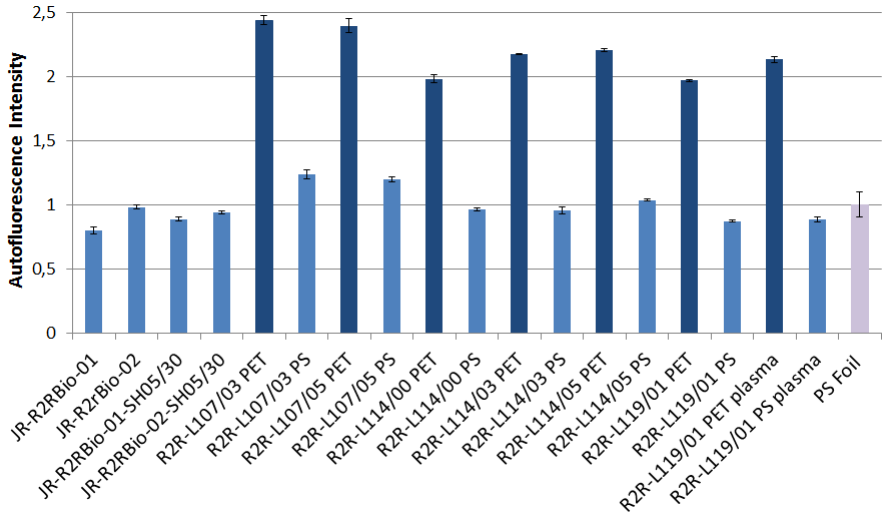

Figure 22: Autofluorescence of resins. Values normalized to background.

Resin thicknesses ranging form 20 to 170 µm compared to PS substrate were imaged

by the fluorescent microscope with excitaion wavelength in wide ultraviolet range. The intensity coming from the resin, regardless of resist layer thickness, was in the range of PS fluorescence, Figures 39, 40, 41 and 42 given in Appendix. From obtained images it is observed that most of the resin do not show a change when layer thickness of the coating is increased. Observed was the border line of the coated and uncoated PS substrate. With increasing layer thickness difficulty of focusing on both surfaces occurs.

4.3 Generation 1

Master with V-grooved channels was made by grey scale lithography (Figure 23). Differently patterned structures that are periodically repeated across 6″coated wafer.

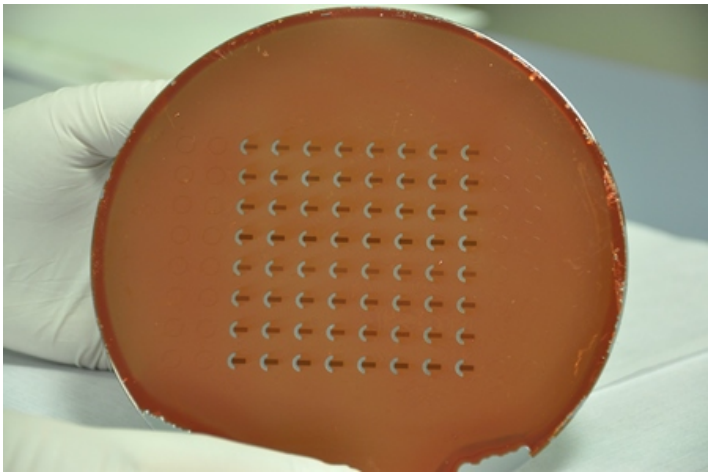

Figure 23: Generation 1 master obtained by maskless lithography.

Information about obtained shape of the V-channels is provided by light microscopy of imprint's cross section after it has been cut by microtome, see Figure 24 **a** and profilometry of the patterned resist within master **b**. Obtained structures' characteristics are given in Table 2.

4.3.1 Capillary Flow within V-Groove Channels

Calculated Capillary Flow

Presented results describe capillary flow within open V-shaped channel, calculated by Rye's model. [30] Calculation was done for three different contact angle of the liquid-

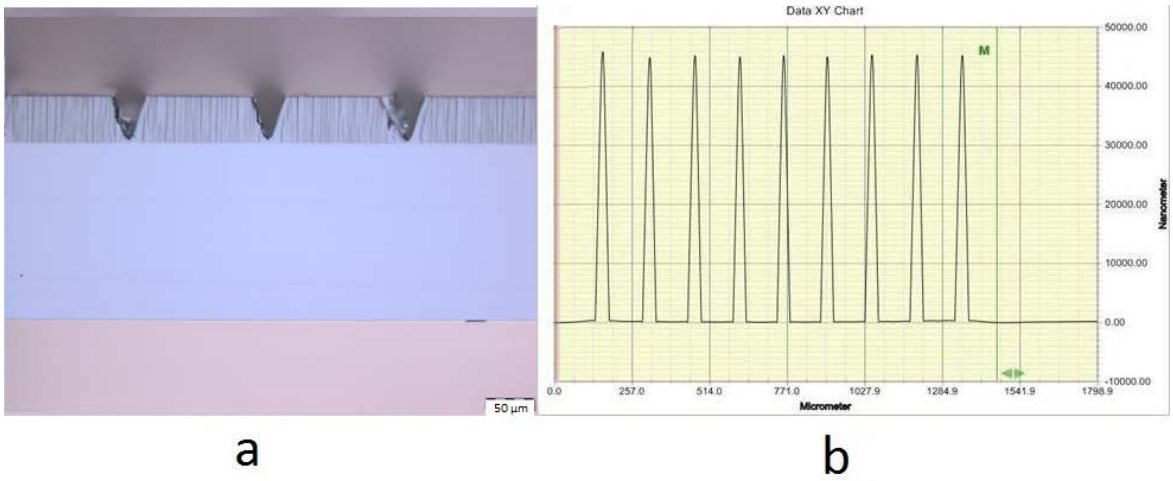

Figure 24: a) Microtomy cross section within channels of generation 1 **b)** profilometer scan.

Table 2: Generation 1 measured features. **C-D**-channel depth, **C-W** channel width, **C-C Distance** distance between channels

Pattern	**Number of Channels**	**V-groove angle** [°]	**C-D** [μm]	**C-W** [μm]	**C-C Distance** [μm]
Structure 1	9	39.4	46	33	115
Structure 2	14	39.4	46	33	65
Structure 3	19	39.4	46	33	38
Structure 4	29	39.4	46	33	17

solid interface, representing three different resins. Channel geometry, out of simplicity, is taken to be perfectly V-shaped with sharp apex angle at the bottom, see Figure 25.

Observed Capillary Flow

Imprints of the generation 1 were taken for the observation of the capillary flow. Goal was to check if the liquid spreads only along V-shaped channel, and which of the four patterns has the best performance to keep the liquid within the channels. Three different resins were used, so that an overview can be gained how different surface energies impact the SCF, (Figure 26). All imprints before use had a shelf life of 1 week.

Best SCF is exhibited for imprint done with JR-R2RBio-02 resin. After the liquid has been deposited, it spreads across all channels equally. Finally, all channels are filled after 20 ms. In case of resin 100SF-XP type G, the liquid does not spread that easily.

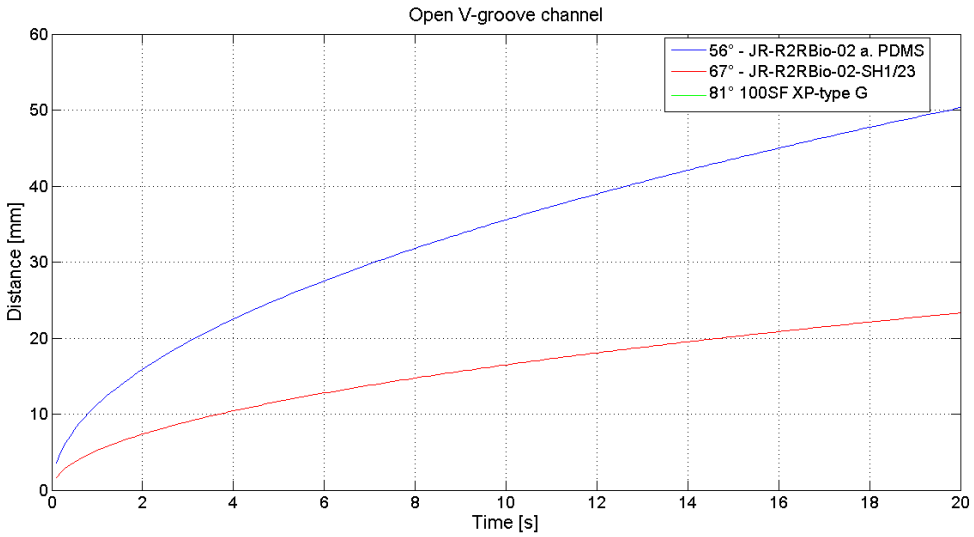

Figure 25: Modelled capillary flow within V-shaped channel. Note that for 100SF-XP type G, theoretically no flow can occur for the measured angle of 81°

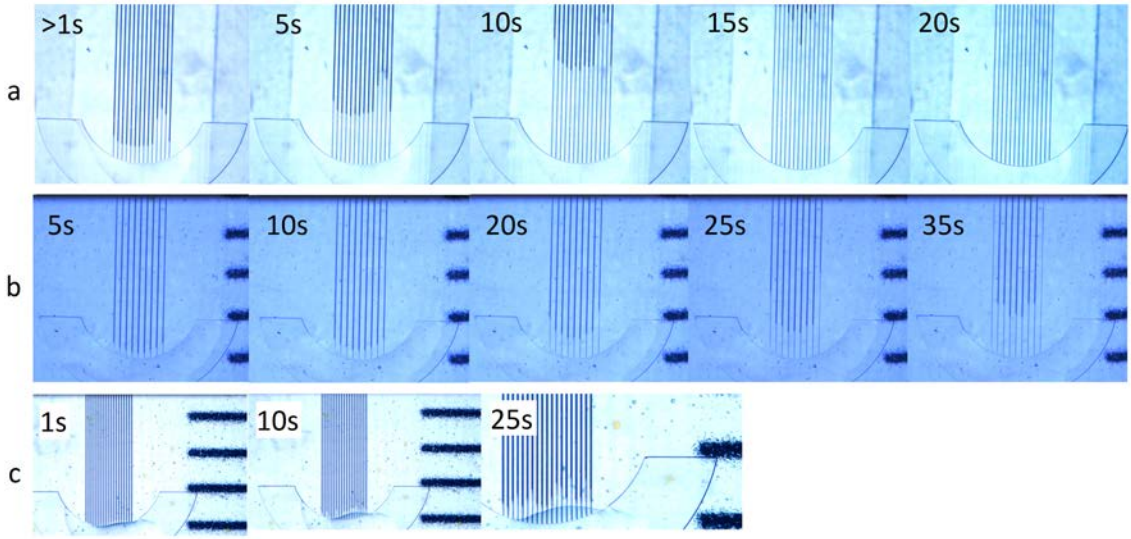

Figure 26: Capillary flow within V-shaped channel in different imprint resins. **a** JR-R2RBio-02, **b** 100SF-XP type G and **c** JR-R2RBio-02_1/23

In the presented Fig. 26b, one can see that liquid did fill the first and the last channel, however, channels in between stay unfilled. Although by theory the SCF for measured contact angle of ∼81° should not even happen, spreading of liquid within channels could be explained by heterogenicity of the resins - local hydrophilic areas. Finally, structured resin JR-R2RBio-1/23 does not show the filling of channels. Liquid that is seen at the beginning of channels, comes from the deposition drop rather than from capillary force

on the liquid from the container. Possible reason for not observing SCF could lay in contact angle of the interface between resin and liquid, as well as mechanical barrier such as air bubbles formation within imprinted resin at the channel surface. Generally observed velocities are not matching the calculated values. This is due to the fact that V shaped channel does not really have ideally sharp apex angle. Curvature radius of the tip of the apex angle is measured to be 1.48 µm. Nevertheless, it is here shown that the liquid does spread within the channel once it the deposited volume exceeds the volume of the channels. The presented sequences in Figure 26 are chosen due to the good video quality of the samples, for all the samples regardless of number of channels (or more specifically distance between the channels) the same behaviour was observed. Regarding issue whether liquid flow follows the channel geometry rather than flooding the top surfaces, practical approach of fluorescent labelled liquid was used, so the coated channels could be observed under fluorescence microscope with excitation wavelength in wide green range, see Figure 27.[†]

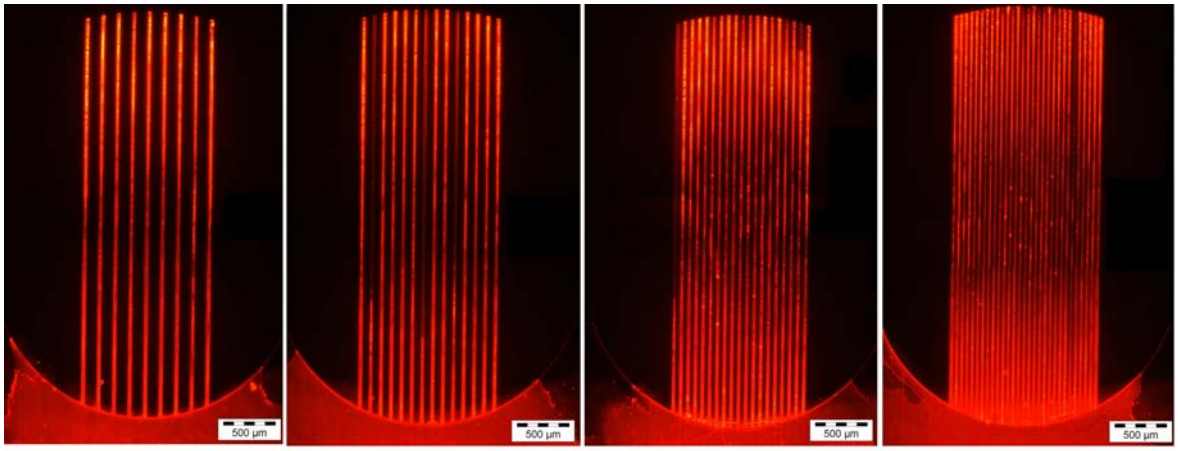

Figure 27: Fluorescence microscope image: Generation 1 (from left to right: structure 1, structure 2, structure 3 and structure 4) imprints coated with Cy3 labelled protein.

For the patterns with longer inter channel distance (Structure 1 and Structure 2) it is clear that the liquid flow is driven only by a capillary force acting upon the liquid within channels. Lowering the distance between the channels (like it is the case for Structure 3 and structure 4) one also lowers the contrast resolution of the microscope.

[†]Due to small field of view of the microscope objective images were stitched together in order to see full length of channels.

Therefore it can not be deducted whether flooding of the top surfaces (at the beginning of the channels) occurs or if it just is the incapability of contrast resolving. Simulation of the fluid flow was conducted by project partner Bionic Surface Technologies GmbH, by computational fluid dynamics method. The results are given within Figure 28.

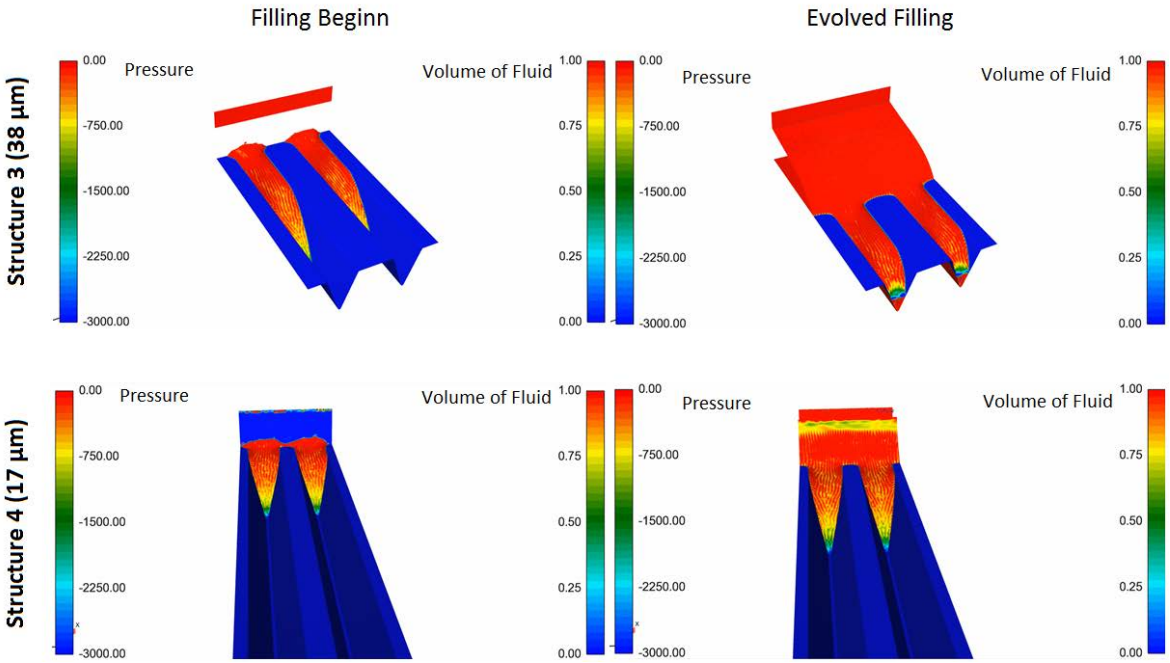

Figure 28: Simulation of the fluid flow of structure 3 (distance between the channels 38 µm) and structure 4 (distance between the channels 17 µm)

Here, it is shown that in case of structure 3, with 38 µm inter channel distance, liquid flow is governed only by the forces arising from channel geometry. However, once the liquid reaches end of the channels, and guiding pressure drops to zero, flooding occurs. In case of structure 4 (17 µm distance between neighbouring channels) the flooding occurs instantly, however, it is less obvious in Figure 28. Liquid surface energy is causing such effect. Decreasing the fluid surface energy and deposition of small volumes deal with the problem of flooding.

4.4 Generation 2

Master with structures of generation 2 contains network of star-like pattern that should promote build up of neuron network, was obtained by UV photolithography.

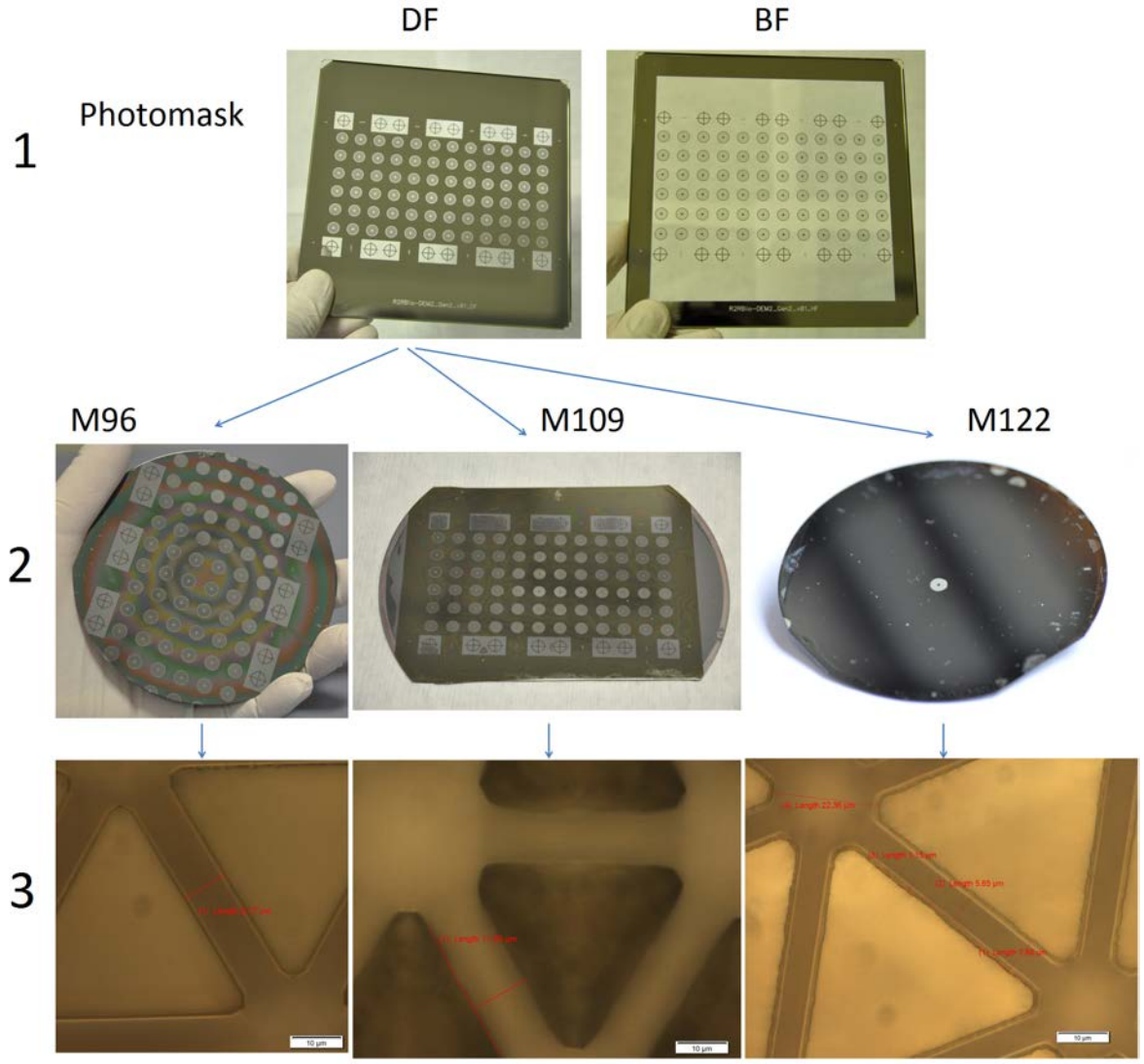

Figure 29: Generation 2. **1** Darkfield and brightfield photomasks, **2** obtained Masters, M96 - hard contact exposure - smallest feature ∼8.77 µm, M109 - flood exposure - smallest feature ∼11.65 µm and M122 - hard contact exposure - with channel width of ∼5.65 µm. **3** Light microscope images with 100 times magnification of each master, respectively.

Mastering

Photomask of size of dimensions of 5″ times 5″contains 72 structures (dimension 6×12) and alignment points, that fit the 96 well microtitter plate, see Figure 29 feature dimensions of the photomask, channel width and length, diameter of the cavity and distance between the cavities are given in Table 3.

Table 3: Feature dimensions of the dark field and bright field photomask.

	Channel		**Cavity**	
	Width [µm]	**Length [µm]**	**Diameter [µm]**	**Distance [µm]**
Structure 1 (DF)	5	50	20	70
Structure 2 (DF)	7.5	75	30	105
Structure 3 (DF)	10	100	40	140
Structure 1 (BF)	5	50	20	70
Structure 2 (BF)	7.5	75	30	105
Structure 3 (BF)	10	100	40	140

Due to lack of an optimal mask holder for the mask aligner EVG 620, area of exposure was not larger than 4 inch in diameter.

Central structures, in respect to wafer, had real hard contact with the photomask, while the peripheral ones, due to bulge formation while spin coating on the very edge of the wafer, haven't been in hard contact with the mask. This applies only for AZ 9269 positive resist. Using solid resist of defined thickness Ordyl SY320 had the advantage that the resist layer is spatially uniform. However, exposed Ordyl SY320 never developed totally, so no master with this resist was used for further work. Transferring full pattern of the photomask onto 6″wafer was done without mask holder, by so called, flood exposure. Even though, it is counted as contact printing, the undefined gap between the resist and mask decreases the resolution. This effect was not specified, but depends on local irregularities of the resist layer. Both masters M96 and M109 were, however, obtained with a too high exposure dose, which also had an impact on the resolution.

To obtain the highest resolution possible, only one structure from the mask (structure with the smallest features) was transferred onto the resist via photolithography. This

was done by blocking the rest of the mask with a aluminium foil. Also the exposure dose was reduced to 1800 mJ/cm^2 as suggested by the manufacturer. The obtained master is depicted in Figure 29.

Table 4: Highest resolution defined through channel width (**C-W**), height represented through wall height (**W-H**) and aspect ratio (AR) obtained via different mastering approaches

	Structure 1			**Structure 2**			**Structure 3**		
	C-W [µm]	**W-H** [µm]	**AR**	**C-W** [µm]	**W-H**[µm]	**AR**	**C-W** [µm]	**W-H** [µm]	**AR**
M96 (4 *Zoll* **wafer)**	8.55	19.8	2.32	11.92	19.8	1.66	13.92	19.8	1.42
M109 (6 inch wafer)	10.35	21.1	2.04	12.52	21.1	1.69	15.47	21.1	1.36
M122 (4 inch wafer)	5.85	22.25	3.8	-	-	-	-	-	

One of the mastering goals was to read a high aspect ratio (AR), which is defined as height over channel width. Profilometery measurement of resist layer thickness i.e. pattern walls height yielded a value of ∼20 µm uniform hight. Due to size of the stylus it was not possible to scan the real profile of the structure, nevertheless, the structure height was easily measured. In the measurement range of 65 µm the manufacturer claims a resolution of 1 µm. The master was observed by light microscopy if the channels are free of the residuals. The curvature radius of the edges was measured with microtomography (Fig. 30). The wall tilting angle both measured and calculated was ∼3 °C, the curvature radius of edges 0.6 µm. Final resolution (given by channel width), structure height and corresponding aspect ratio for three mastering approaches is listed in Table 4.

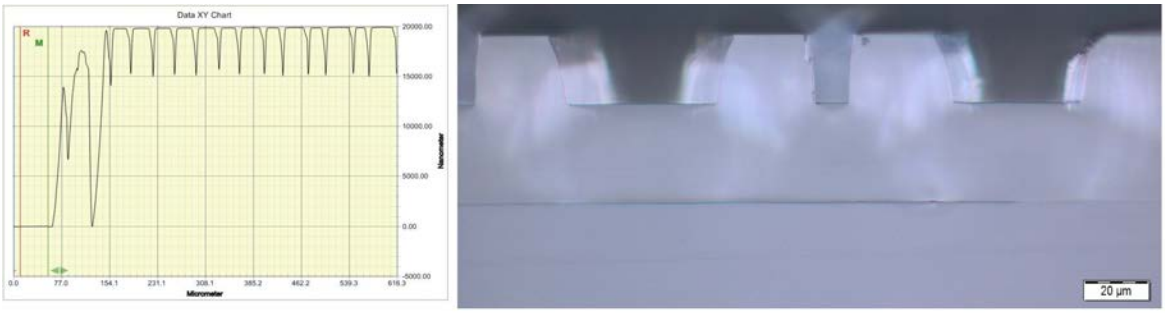

Figure 30: Profile of the master M96. **a)** Profilometer mesurement within pattern, **b)** microtome cross section of the imprint with BPA(EO)$_{10}$DA resin on PS substrate.

Table 5: Volume within rectangular channels for structure height of 20 µm.

	Structure 1	**Structure 2**	**Structure 3**
Total Area [10^6 µm^2]	5.01	5.01	5.01
Volume [10^6 µm^3]	100	100	100
Volume [µl]	0.1	0.1	0.1
Factorized Container Volume	6.26	6.25	6.25

4.4.1 Volume of the patterned Surface

To estimate the liquid volume needed for channel coating, the total volume of channels and cavities has to be calculated. As template a structure of 20 µm height and ideally transferred mask dimensions was taken. It is shown that the channels and cavities of all three structures have the same volume, see Table 5. Structures of generation 2 contain a central container of 1 mm diameter. Its' volume, in case of 20 µm walls height, is 0.018 mm^3.

Since, no master with walls of 0° tilting angle was manufactured, volume of the trapezoidal channels was calculated. However, this calculation assuming a width of the channel bottom corresponding to the mask (Table 6).

Table 6: Volume within trapezoidal channels (wall tilting angle 3°C) for structure height of 20 µm.

	Structure 1	**Structure 2**	**Structure 3**
Total Area [10^6 µm^2]	5.01	5.00	5.01
Volume [10^6 µm^3]	113	109	106
Volume [µl]	0.1	0.1	0.1
Factorized Container Volume	7.1	6.8	6.7

4.4.2 Wetting Transitions

The wettability of the patterned surface varied depends on the used imprint resist. The measured transition energies ranged from Cassie-Baxter to Wenzel state. Obtained values for the energy transition barrier for different contact angles are given in Table

7.

Table 7: Energy transition barrier for different contact angles. JR-R2RBio-02 imprinted against different template materials.

Resin Code	**Contact Angle**	**Structure 1**	**Structure 2**	**Structure 3**
	[°]	ΔE_1 [mN/m]	ΔE_2 [mN/m]	ΔE_3 [mN/m]
JR-R2RBio-02 (a. N2)	42	-84.025	-56.086	-42.012
JR-R2RBio-02 (a. Ni)	48	-56.221	-37.529	-28.112
JR-R2RBio-02 (a. Al)	53	-33.834	-22.587	-16.919
JR-R2RBio-02 (a. PDMS)	60	-16.917	-11.293	-8.459

Regardless of the aspect ratio transition from Cassie-Baxter to Wenzel state will occur. Negative sign of ΔE suggests that at deposition the system is at the state of higher energy. Wettability is strongly dependent on surface energy, meaning that if the surface is hydrophilic transition from not wetted to fully wetted state is bound to happen.

4.4.3 Roll-2-Roll Imprinting

Changing parameters (velocity and pressure) during R2R process had an impact on the quality of the imprints. Best imprints were obtained with R2R 2 m/min with pressure against imprinting roll set to 0.1 bar. Concerning pattern size, the best imprinted structures were the largest ones, regardless of the imprinting speed and pressure. The smallest structure showed the most formation of air bubbles. The problem of air bubbles was decreasing by speeding up and adding pressure, however, for the smallest structure it was always present, while for the largest structure it was diminishing. It remains unclear whether the problem arises during R2R imprinting or on the Al shim was already imperfect (data will follow).

Figure 31 **1** shows the imprinting evolution of the smallest featured pattern of the generation 2, second and third picture (going from left to right) show almost no defect. It is to be noted that extruded parts of the pattern did not get filled by the resin. Bellow v=2 m/min and p=0.1 bar the desired structures are formed however only locally. Regarding structure 2 (medium feature size) similar behaviour is observed, see Figure 31 **2**. Applying pressure against the mold, suppressed forming of air bubbles. However, at lower speeds (0.5 and 1 m/min) air bubbles were trapped within triangular

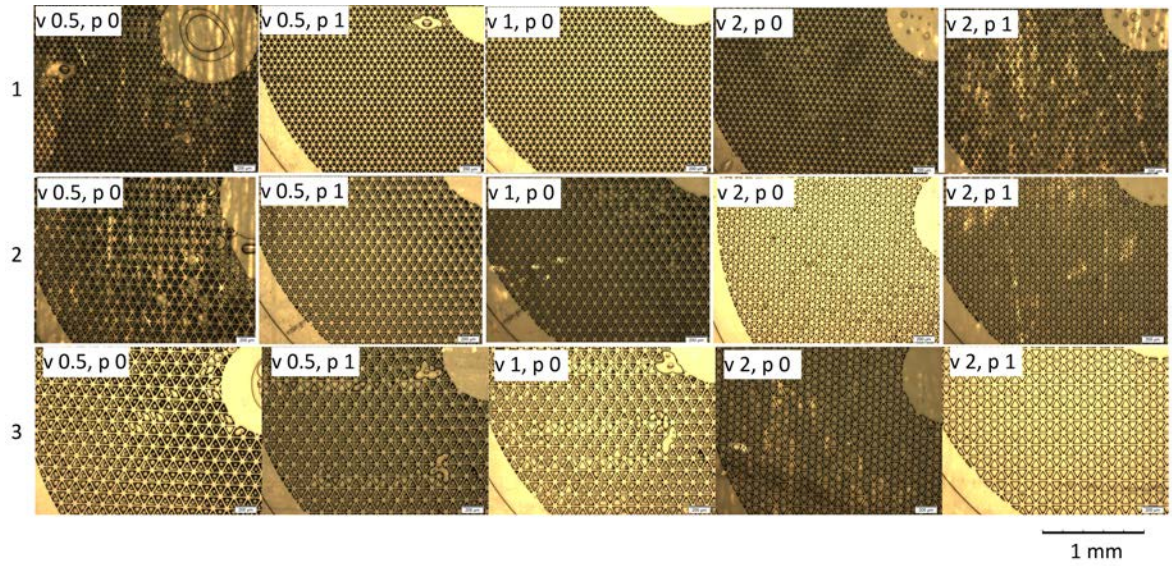

Figure 31: Improvement of imprinting quality by changing parameters of R2R speed v given in min/m , and pressure p against the imprinting roll in bar. **1)** Structure 1 -smallest features, **2)** Structure 2 - middle feature size, **3)** Structure, 3 largest features.

pillars. Increasing velocity improved imprinting of feature, however, best improvement was observed for structure 3 (largest features), see Figure 31 **3**.

Not only does the air bubble problem disappear by increasing the speed and adding pressure, also the appearance of random defects decreases. Al shim has been used for making somewhat 30 imprints, before starting to fall apart. Imprints containing Al residue provide information on state of the Al shim. Aluminium residue was, however, also visible on one of the first imprinted structures. This suggests, that the adhesion of the aluminium on to the PUA imprint was to low.

4.4.4 Observed Capillary Flow Rectangular Channels

The condition for spontaneous capillary force within an open rectangular channel is given in Figure 32. The capillary flow within a channel with AR of 1 occurs for contact angles lower than $\sim 65°$. With raising aspect ratio, it is possible to use liquids with larger contact angles.

Observation of SCF within rectangular channels was done for both confined and open channels. Confining channels was done by thin PS foil with a laser cut opening above the container needed for liquid deposition. While confined channels easily get filled due

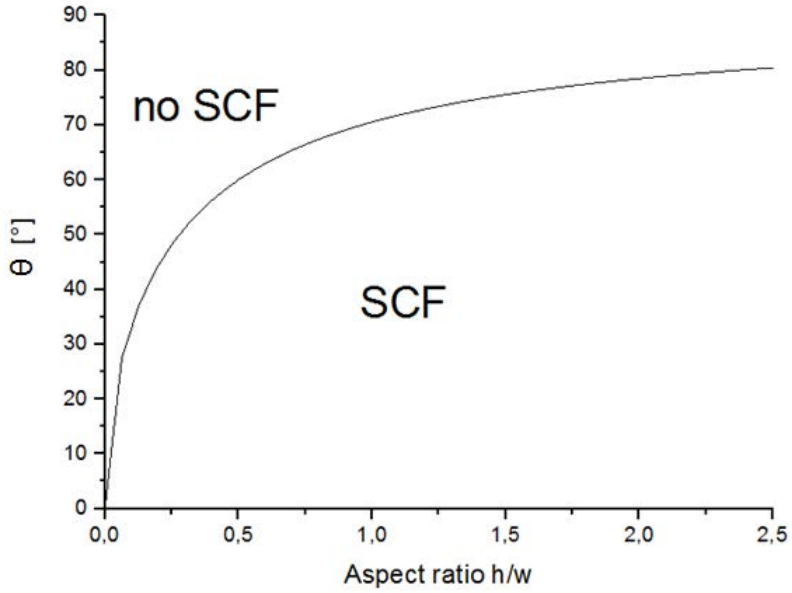

Figure 32: Condition for spontaneous capillary flow within open rectangular channel as a function of aspect ratio.

to channel size, filling of open channels depends strongly on advancing contact angle between surface and deposited liquid. Drawback of confined channels is air trapping which disables filling of the whole pattern, see Figure 33. Presented is the imprint in JR-R2RBio-02 cured against PDMS under air and the liquid used was coloured water filtered with 0.2 µm filter.

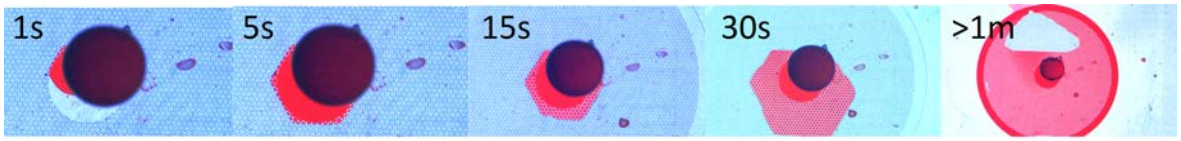

Figure 33: Capillary flow observed within confined rectangular channels. Channels confined by microscope cover glass. Note that the container diameter measures 1 mm.

In case of open channels for the same imprint no capillary force was observed. Deposited drop stayed at the place of deposition. Reducing contact angle at the solid-liquid interface by adding ethanol to the coloured solution as well as imprinting against metallic surface showed improvement. Resins imprinted by R2R imprinting technique were taken and tested for SCF within open channels. Whole pattern got filled within less than 30 seconds, see Figure 34. The filling of channels is easiest to observe when

the deposited volume is the same ar less than the size of the container volume.

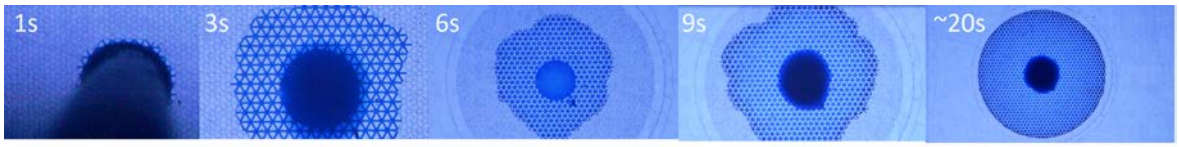

Figure 34: Capillary flow within open rectangular channels of imprint obtained by R2R NIL (Structure 3). Note that container diameter measures 1 mm.

The observed capillary flow rates correlate with the criterion in Fig. 32. It is the cavity size that reduces the capillary flow due to its width - i.e. lower aspect ratio. For example, given the aspect ratio for cavity 0.43 is rather low, however with reduced contact angle ($\sim$43°) due to imprinting against Aluminium and ethanol content of working fluid, the low aspect ratio does not have a large impact on the filling of the channels. Interestingly, structure 1 R2R imprints were showing fluid flow within channels of imperfect walls and even a very low aspect ratio.

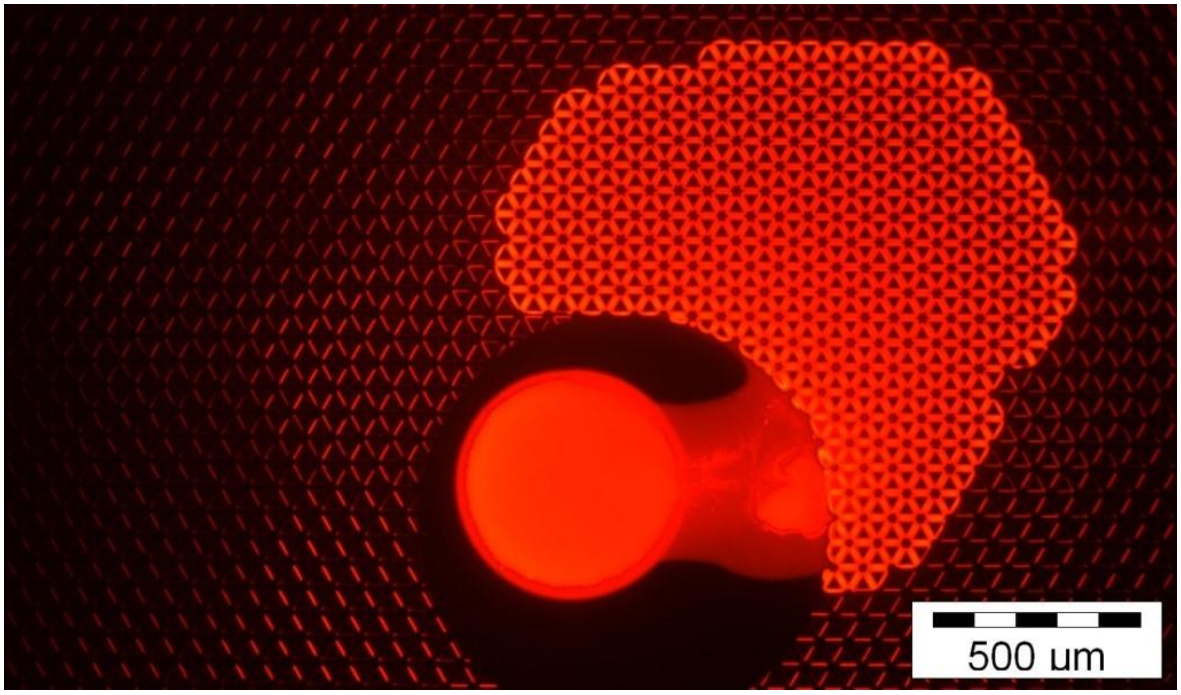

Figure 35: Capillary flow of BSA Cy3 labelled protein within open rectangular channel.

Also in this case, fluorescence microscopy was used in order to determine that liquid flow happens only within channels. Adjusting the depositing volume to the container

volume has shown to yield huge improvement to the capillary filling of the channels as well as avoiding flooding of the top structures. Deposition of BSA Cy3 labelled protein of 1 mg/ml concentration was deposited into container by microspotter. Volume deposited was 16 nl which matches the container volume. The reason why the container does not look filled is that if deposition always takes place at the same point, it is the deposited drop that swells, rather than that the container gets filled. Nevertheless, the flow within channel was observed, see Figure 35. In Fig. 35 it seems as if cavities did not get coated by the BSA Cy3. However, this effect arises out of contrast coming from channels - smallest feature of the pattern - which yields the highest intensity. Due to high viscosity of the BSA solution, filling of the full pattern was not achieved.
Coating by protein solution for neuron cell adhesion improvement, is a delicate step that should assure equal concentration distribution of adherent molecule within channels. Finding the ideal protein is still under research. Dispensing just the right amount of solution is guaranteed by low volume dispensers like microspotting or inkjet printing. For high throughput inkjet printers were already shown as a successful tool for depositing small volume proteins by means of automated process.[14]

4.4.5 Generation 2.1

Manufacturing of master of generation 2.1 was done on 2 inch wafer coated by AZ 9260 by grey scale lithography. This master contains two patterns, with interconnected cavities, one within six inlets, the other with four inlets, see Figure 36. Additional difference with respect to the generation 2, is that the channel geometries vary both in depth and width inbetween two cavities. Obtained channel width (W) and depth (H) are given in Table 8:
Although aimed for V-shaped channels, obtained apex angle had rather large curvature radius. However, due to scaling of the topography graph obtained by profilometry, curvature of the apex angle was not observed, see Figure 37a. Better view was obtained from imprint cut by microtome (37b), as well as looking at the PDMS mold under scanning electron microscope (SEM) with 45° tilting angle, yielded information that the channels were rather rounded than V-shaped, see Figure 37 c1 and c2. This, of course, has huge impact on SCF. The estimated curvature radius at the apex angle was

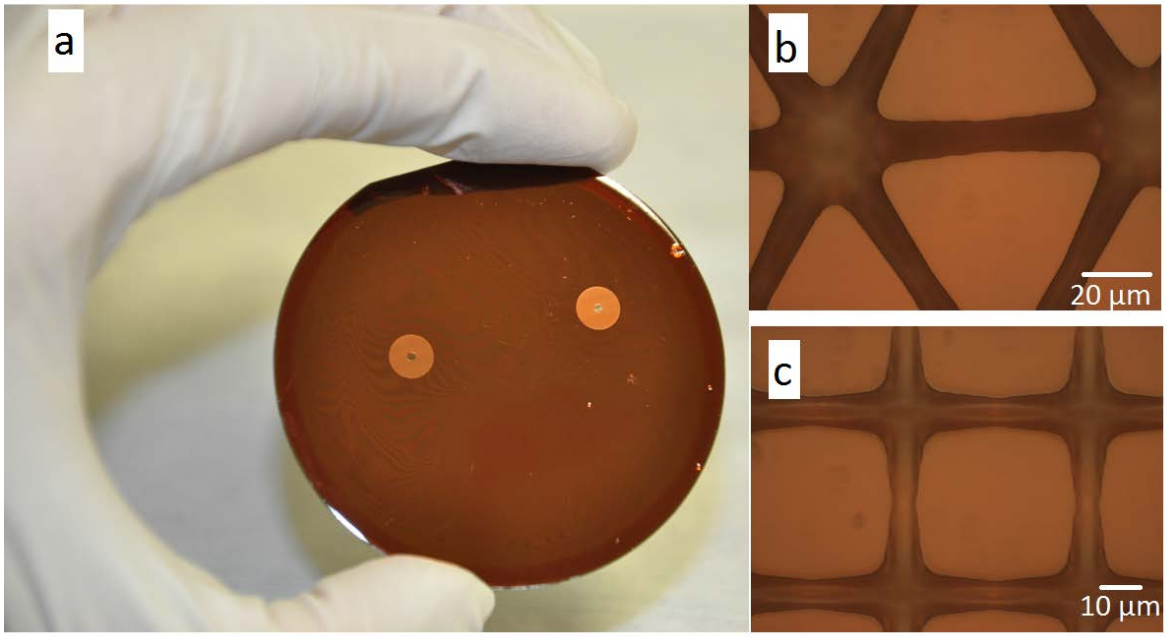

Figure 36: a) Master of generation 2.1. **b)** Pattern with six inlets, **c)** Pattern with four inlets

Table 8: Pattern feature size of generation 2.1.

Pattern	**Cavity**		**Channel front**		**Channel middle**	
	W $[\mu m]$	**D** $[\mu m]$	**W** $[\mu m]$	**D** $[\mu m]$	**W** $[\mu m]$	**D** $[\mu m]$
six inlets	31.2	19.8	12.24	9.67	8.42	6.67
four inlets	19.96	11.6	10.61	6.60	6.09	4.90

∼6 µm within the cavity, ∼7 µm within frontal part of the channel and ∼4 µm within middle of the channel. Large curvature of radius for the of the bottom apex angle has an impact on the Concus-Finn condition, see Equation 38.

4.4.5.1 Capillary flow of V-shaped channels

After deposition of the liquid into the container in case of open channels, no spontaneous capillary force was observed. This observation is explained by unfulfilled Concus-Finn condition as well as low aspect ratio of the obtained pattern. In case of confined channels, capillary force is observed, however, due to the large contact angle of liquid with confinement foil (measured angle of the liquid-foil interface ∼123°), capillary filling was rather slow. In Figure 38 the state of filling of the pattern after aprox. 1

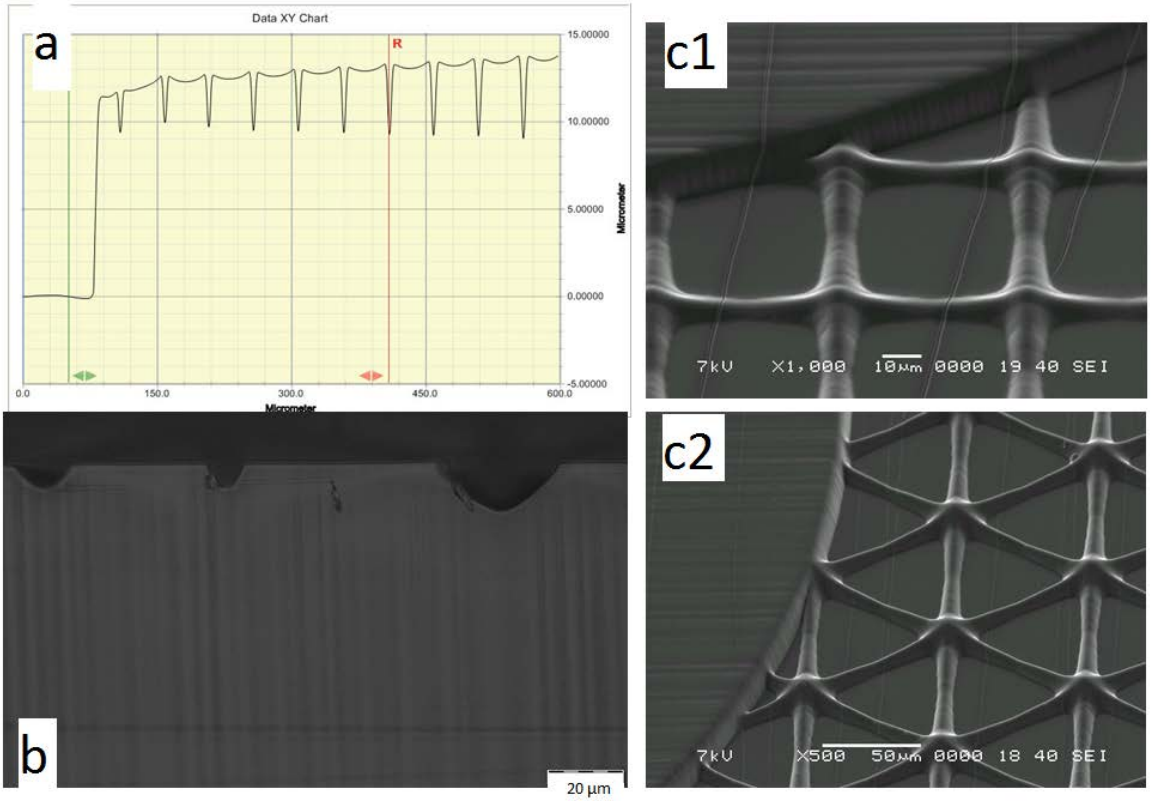

Figure 37: a) Profilometry scan **b)** Microtomy cross section under light microscope, **c1)** SEM image pattern six inlets, **c2)** SEM image pattern four inlets.

minute is given.

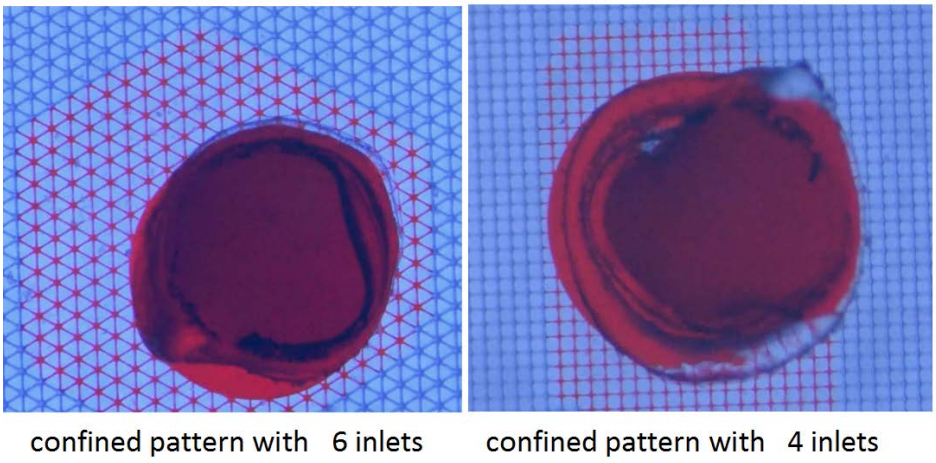

Figure 38: 1 minute after liquid deposition: filling of the generation 2.1 pattern

5 Conclusions

Scope of this work was to manufacture patterns as well as to develop strategies needed for spontaneous capillary flow. It has been shown that the structures up to an aspect ratio of 3.8 (5.85 µm channel width, and 22.3 µm wall height) could be obtained by hard contact photolithography, proving its high resolution on a microscale. Nevertheless, spatial resolution obtained by photolithoraphy depends highly on the quality of the deposited resist layer. Additionally, the utilized alignment system can not provide optimal resolution for large area microscale. Difficulty of preforming high resolution photolithography on a large are was already reported in literature.[8] This suggests that fabrication of 96 patterns (to fill the wells of 96 microtiter plate) is easier by means of step and repeat nanoimprint lithography. Regarding capillary filling of the channels it was observed that adjusting the volume of the working fluid to the container volume improved the filling performance. While generation 1 has containers larger than the total channel volume, containers of the generation 2 are smaller by the factor of 6. However, in both cases containers are too large, and occupy a lot of space. Especially the one of the generation 2 is unfavourable, since it occupies the most important part of the well, where large area of neural monolayer could grow. Concerning the capillary flow, both confined and open channels have their advantages. For example, confined channels have longer shelf-life and easier exhibited capillary flow. On the other hand this would imply additional manufacturing steps - increase of damage probability and obliging the customer to attach the patterned foil on his own is rather disadvantageous. Manufacture of open structures might need additional work for lowering the contact angle of the coating protein with the imprinting resin, but is however advantageous.
Low autofluorescence of all considered resins on a PS foil prove that all of them could be considered from the point of view of the fluorescence microscopy. Once the biological requirements of compatibility and toxicity and chemical and physical stability are fulfilled, it would be of advantage that the resin's refractive index matches the one from the polystyrene, in order to lose the less light possible while performing microscopy. Considering all requirements the resin with the sample code JR-R2RBio-02 is until now the optimal candidate for imprinting. Alternatively, protein coating should pro-

vide the missing optical thickness. This also applies for the form of the channels, i.e. even though V-shaped channel have an advantage when it comes to chemical patterning, it contributes more to light reflection, decreasing the light intensity coming from the probe (neural cells).
Optimizing the aspect ratio and lowering the surface tension of the coating solution, guaranties possibility of channel coating by means of capillary force. Imprinting against metallic surface of the R2R mold puts this technique in front when it is aimed for high throughput. Within this work R2R imprinting was used only once, which limits the quality analysis on a larger number or with different masters (of better resolution).

It has been reported that the surface coated by PLL provides good environment for neural cells so these can adhere and grow. Finally, since the project is not fully conducted yet, there are no results on how do neural cells react to topographical surface patterns. Having a feedback of that kind, would, of course, be of great interest.

References

[1] Brechungsindex von Ester, Melinex, Mylar. 25.01.2017 Retrived form http://www.filmetrics.de/refractive-index-database/PET/Estar-Melinex-Mylar.

[2] Refractive index database. 25.01.2017 Retrived from http://refractiveindex.info/?shelf=3d&book=plastics&page=ps.

[3] The solution in energy curing. Energy curing products. Tech. rep., Miwon Specialty Chemical Co., Ltd., 2009.

[4] Amirtha Rammohan, Prabhat K. Dwivedi, Rodrigo Martinez-Duarte, Hari Katepalli, Marc J. Madou, and Ashutosh Sharma. One-step maskless gayscale lithography for the fabrication of 3-dimensional structures in su-8. *Sensors and Actuators B: Chemical 153* (2011), 125–134.

[5] Andersson, H., and van den Berg, A., Eds. *Lab-on-Chips for Cellomics*. Kluwer Academic, 2005.

[6] Artira Ghosh, Ranjan Ganguly, Thomas M. Schuzzius, and Constantine M. Egaridis. Wettability patterning for high-rate, pumpless fluid transport on open, non-planar microfluidic platforms. *Lab on a Chip 14* (2014), 1538.

[7] Assaf, Y., Blumenfeld-Katzir, T., Yovel, Y., and Basser, P. J. Axcaliber: a method for measuring axon diameter distribution from diffusion mri. *Magnetic resonance in medicine 59*, 6 (2008), 1347–1354.

[8] B Gorzolnik, P Mela, and M Moeller. Nano-structured micropatterns by combination of block copolymer self-assembly and uv photolithography. *Nanotecnology 17* (2006), 5027–5032.

[9] C Peroz, S Dhuey, M Volger, Y Wu, D Olynick, and S Cabrini. Strep and repeat uv nanoimprint lithography on pre-spin coated resist film: a promising route for fabricatin nanodevices. *Nanotecnology 21* (2010).

[10] Chris A. Mack. Resolution and depth of focus in optical lithography. *Microlithographic Techniques in IC Fabrication, SPIE 3183* (1997), 14–27.

[11] D. J. Wagner, and A. H. Jayatissa. Nanoimprint lithography: Review of aspects and applications. *Proc. of SPIE 6002* (2005).

[12] D. Kleinfeld, K. H. Kahler, and P. E. Hockberger. Controlled outgrowth of dissociated neurons on petterned substrates. *The Journal of Neuroscience 8(11)* (1988), 4089–4120.

[13] Daiki Murakami, Hiroshi Jinnai, A. Wetting transition from cassie-baxter state to the wenzel state on textured polymer surfaces. *Langmuir 30* (2014), 2061–2067.

[14] E. A. Roth, T. Xu, M. Das, C. Gregory, J. J. Hickman, and T. Boland. Inkjet printing for high-throughput cell patterning. *Biomaterials 25* (2004), 3707–3715.

[15] F. Hejda, P, Solar, J. Surface free energy determination by contact angle measurements - a comparison of various approaches. *WDS'10 Proceedings of Contributed Papaers Part III* (2010), 25–30.

[16] Fatima H Labeed, H. O. F., Ed. *Microfluidic n Detection Science*. Royal Society of Chemistry, 2015.

[17] Gerlach, G., and Dtzel, W. *Introduction to Microsystem Technology. A Guide For Students*. John Wiley & Sons, Ltd, 2006.

[18] Guo, L. J. Nanoimprint lithography: Methods and material requirements. *Advanced Materials 19* (2007), 495–513.

[19] Helmut Schift. Nanoimprint lithography: An old story in modern times? a review. *Journal of Vacuum Science and Technology B 26* (2008).

[20] Hiroshi Miyajima, and Mehran Mehregany. High-aspect-ratio photolithography for mems applications. *Journal of Microelectromechanical Systems 4* (1995).

[21] Hiroshi Yoshikawa, Jun Taniguchi, Go Tazaki, and Toshiyuki Zento. Fabrication of high-aspect-ratio pattern vie high throughput roll-to-roll ultraviolet nanoimprint lithography. *Microelectronic Engineering* (2013).

[22] Iannone, E., Ed. *Labs on Chip Principles, Design and Technology.* Taylor and Francis, 2015.

[23] J. Berthier, D. Gosselin, N. Villard, C. Pudda, F. Boizot, G. Costa, and G. Delapierre. The dynamics of spontaneous capillary flow in confined and open microchannels. *Sensors and Trasducers 183* (December 2014), 123–128.

[24] J. Berthier, D. Gosselin, E. A generalgeneral of the lucas-washburn-rideal law to composite microchannels of arbitrary cross section. *Microfluidics and Nanofluidics 19* (2015), 497–507.

[25] J. Koch, E. Fadeeva, M. Engelbrecht, C. Ruffert, H.H. Gatzen, A. Ostendorf, and B.N. Chichov. Maskless nonlinear lithography with femtosecond laser pulses. *Applied Physics A 82* (2006), 23–26.

[26] Jacob John, YuYing Tang, Jonathan P Rotshstein, James J Watkins, and Kenneth R Carter. Large-area, continuous roll-to-roll nanoimprinting with pfpe composite molds. *Nanotecnology 24* (2013).

[27] Jean Barthier, P. S. *Microfluidic for Biotechnology.* Artech House, 2010.

[28] Jean Berthier, Kenneth A. Brakke, and Erwin Berthier. A general condition for spontaneous capillary flow in uniform cross-section microchannels. *Microfluidics and Nanofluidics 16* (2014), 779–785.

[29] Jean Berthier, Kenneth A. Brakke, E. B. *Open Microfluidics.* Wiley, 2016.

[30] Junfei Tian, Dushmantha Kannangara, Xu Li, and Wei Shen. Capillary driven low-cost v-groove microfluidic device with high sample transport efficiency. *The Royal Society of Chemistry 10* (2010), 2258–2264.

[31] Larry Thompson, Grant Wilson, M. B., Ed. *Introduction to Microlithography.* American Chemical Society, 1983.

[32] Lars Lauer, Christoph Klein, and Andreas Offenhuser. Spot compliantneuronal networks by structure optimized micro-contact printing. *Biomaterials 22* (2001), 1925–1932.

[33] Letourneau, P. Cell-to-substratum adhesion and gidance of axonal elongation. *Developmental Biology 44* (1975), 92–101.

[34] Li, P. C. H. *Microfluidic Lab-on-a-Chip for Chemical and Bilogical Analysis and Discovery*. Taylor and Drancis, 2005.

[35] M. Otto, M. Bender, F. Richter, B. Hadam, T. Kliem, R. Jede, B. Spangenberg, and H. Kurz. Reproducibility and homogeneity in step and repeat uv-nanoimprint lithography. *Microelectronic Engineering 73-74* (2004), 152–156.

[36] Michail E. Kavousanakis, Carlos E. Colosqui, A. Engineering the geometry of stripe-patterned surface toward efficient wettability wswitching. *Colloids and Surfaces A: Physicochemical and Engineering Aspects 436* (2013), 309–317.

[37] Myra Kitron-Belinkov, Abraham Marmur, Thomas Trabold, and Gayatri Vjas Dadheech. Groovy drops: Effect of groove curvature on spontaneous capillary flow. *Langmuir 23* (2007), 8406–8410.

[38] Nianzhen Li, A. Integration of topografical and biochemical cues by axons during growth on microfabricated 3- d substrates. *Experimental Cell Research 311* (2005), 307–316.

[39] Oliver Geschke, Henning Klank, P. T., Ed. *Microsystem Engeneering of Lab-on-a-chip Devices*. Wiley-VCH, 2004.

[40] Pontus Forsberg, Frederik Nikolajeff, M. Cassie-wenzel and wenzel-cassie transitions on immersed sypoerhydrophobic surfaces under hydrostatic pressure. *Soft Matter 7* (2011), 104–109.

[41] R. R. Rye, J.A. Mann, F. The flow of liquids in surface grooves. *Langmuir 12* (1996), 555–565.

[42] Rajesh Menon, Amil Patel, Dario Gil, and Henry I. Smith. Maskless lithography. *Materials Today* (2005).

[43] Reinhard Lipowsky. Morphological wetting transitions at chchemical sstructure surfaces. *Current Opinion in Colloid & Interface Science 6* (2001), 40–48.

[44] Roar R. Sondergaard, Markus Hrsel, and Frederik C. Krebs. Roll-to-roll fabrication of large area functional organic materials. *Journal of Polymer Science Part B: Polymer Physics* (2012).

[45] Sangeeta N Bhatia, D. Microfluidic organs-on-chips. *Nature Biotechnology* (2014).

[46] Se Hyan Ahn, and L. Jay Guo. Large-area roll-to-roll and roll-to-plate nanoimprint lithography: A step toward high-throughput application of continuous nanoimprinting. *American Chemical Society Nano 3* (2009), 2304–2310.

[47] Shunsuke Chatani, Christopher J. Kloxin, and Christopher N. Bowman. The power of light uin polymer science: photochemical preocesses to manipulate polymer formation, structure and properties. *Polymer Chemistry 5* (2014), 2187.

[48] Tian, W.-C., and Finehout, E., Eds. *Microfluiics for Biological Applications*. Springer, 2008.

[49] Todd M Squires, S. Microfluidic: Fluid physics at the nanoliter scale. *Reviews of Modern Physics 77* (2005).

[50] Torres, C. M. S., Ed. *Alternative Lithography. Unleashing the Potentials of Nanotecnology*. New York. Kluwer Academic/Plenum, 2003. pp. 36-41.

[51] Y. Nam, J. Chang, D. Khatami, G. J. Brewer, and B. C. Wheeler. Patterning to enhance activity of cultured neurona networks. *IEE Proceedings. Nanobiotechnology 151* (2004).

[52] Yaksel Temiz, Robert D. Lovchik, Govind V. Kaigala, and Emmanuel Delamarche. Lab-on-a-chip: How to close and plug the lab? *Microelectronic Engineering 132* (2015), 156–175.

[53] Youngtae Cho, Sin Kwon, Jung-Woo Seo, Jeong-Gil Kim, Jung-Woo Cho, Jung-Woo Park, Hyuk Kim, and Sukwon Lee. Developement of large area nnanoimprint technology by step and repeat process and pattern stitching technique. *Microelectronic Engineering 86* (2009), 2417–2422.

Appendix

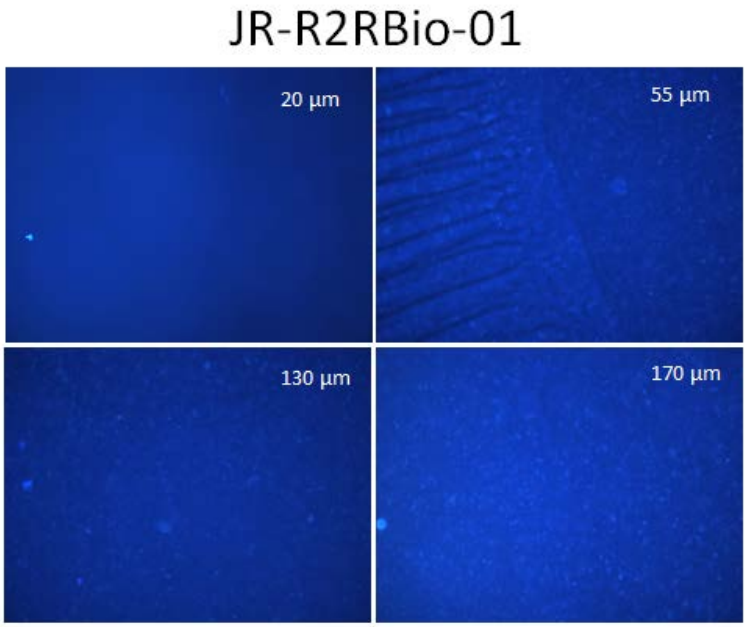

Figure 39: JR-R2RBio-01 resin. Autofluorescence of four different resin thicknesses coated on a PS substrate.

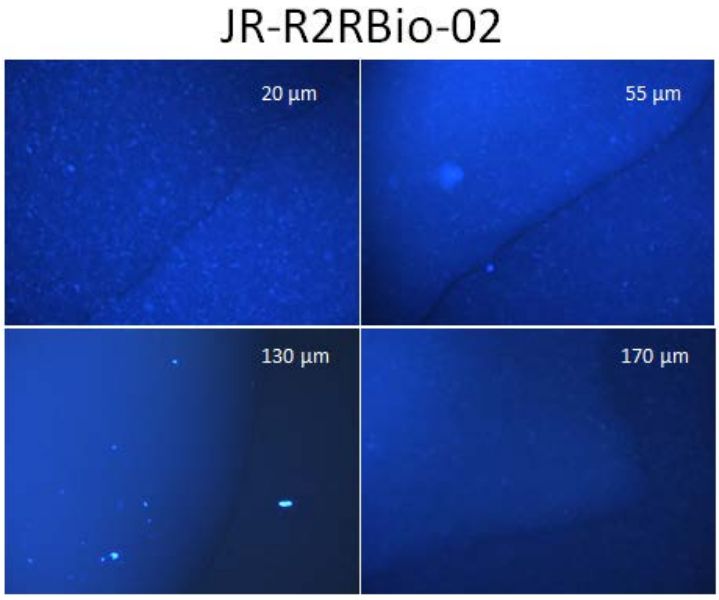

Figure 40: JR-R2RBio-02 resin. Autofluorescence of four different resin thicknesses coated on a PS substrate.

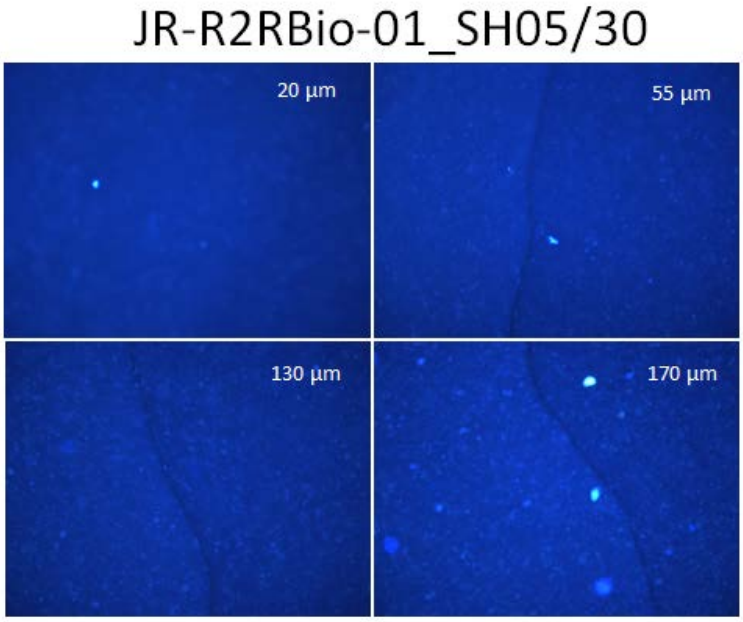

Figure 41: JR-R2RBio-01_SH05/30 resin. Autofluorescence of four different resin thicknesses coated on a PS substrate..

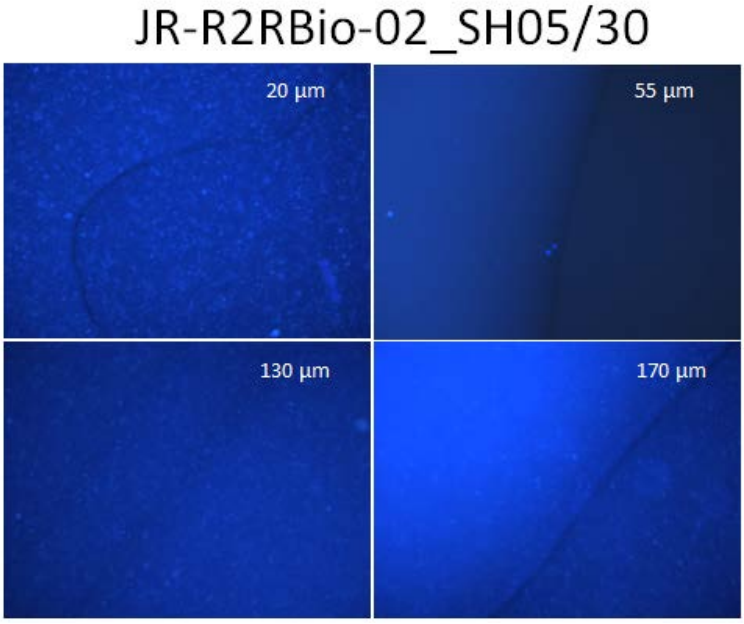

Figure 42: JR-R2RBio-02_SH05/30 resin. Autofluorescence of four different resin thicknesses coated on a PS substrate.

Declaration of Authorship

I hereby confirm that I have authored this Master's thesis independently and without use of others than the indicated sources. All passages which are literally or in general matter taken out of publications or other sources are marked as such.

Vienna, 3rd of March 2017

Minja Čelikić